SIMULATION OF THE ION-BEAM-DRIVEN DRIFT

INSTABILITY IN A MAGNETIC TRAP II

by

V. A. Thomas, and W. M. Nevins

Memorandum No. UCB/ERL M84/46

13 June 1984

ELECTRONICS RESEARCH LABORATORY

College of Engineering University,
University of California, Berkeley, CA 94720

SIMULATION OF THE ION-BEAM-DRIVEN DRIFT

INSTABILITY IN A MAGNETIC TRAP II

by

V. A. Thomas, and W. M. Nevins

ELECTRONICS RESEARCH LABORATORY

College of Engineering
University of California, Berkeley
94720

Simulation of the Ion-Beam-Driven Drift Instability in a

Magnetic Trap II.

V. A. Thomas

Electronics Research Laboratory, University of California,

Berkeley, Ca 94720

W. M. Nevins

Lawrence Livermore National Laboratory, University of California,

Livermore, Ca 94550

ABSTRACT

Recent Experiments on the TMX-U device at LLNL have indicated the possibility of a low frequency ($\omega << \Omega_{ci}$) drift wave being driven unstable by the injection of neutral beams in the thermal barrier region. Nonlocal linear theory is performed for this instability using slab geometry and the electrostatic approximation. Particle simulations are used to verify the linear theory and to recover relevant nonlinear phenomena. Important nonlinear effects include: (1) E×B trapping (2) relaxation of the beam density profiles , and (3) weakly nonlinear electrons ($e\delta\phi/T_e \simeq 0.1$). These nonlocal simulations are compared with previous simulations of Ref. 1. which used a local approximation for the

Simulation of the Ion-Beam-Driven Drift Instability in a

Magnetic Trap II.

V. A. Thomas

Electronics Research Laboratory, University of California,

Berkeley, Ca 94720

W. M. Nevins

Lawrence Livermore National Laboratory, University of California,

Livermore, Ca 94550

1. Introduction

Drift waves have long been an area of major activity in the controlled fusion community. In particular particle simulation techniques have been used many times to examine some drift waves in great detail[2-7]. In this paper a relatively new type of drift wave instability is examined. This paper is motivated by some recent experiments on TMX-U that have indicated that electrostatic drift waves may be driven unstable by injection of neutral beams in the thermal barrier region[1]. The linear theory and the particle simulations in Ref. 1 were performed using the local approximation. The purpose of this paper is to relax the local approximation in both the theoretical treatment and in the particle simulations.

Section 2 describes the model equilibrium which uses a slab model with a uniform magnetic field together with the electrostatic approximation. Section 3 describes the linear nonlocal

analysis, the simulation techniques, and the linear simulation behavior. Section 4 describes the dominant nonlinear behavior from the particle simulations and includes a discussion of the dominant effect, which is $E \times B$ trapping[8]. Section 5 contains a brief summary of the major results.

2. Model Equilibria

The geometry for the model is given in Fig. 1. The equilibrium density gradient is perpendicular to the magnetic field. There may be an equilibrium electric field in the x direction. The low beta approximation is made, which makes it possible to take B_0 as independent of the x coordinate. The beam velocity parallel to the magnetic field U_b is taken to be much less than the Alfven speed V_A. Under these conditions for the beam velocity and the Alfven speed the electrostatic approximation may be employed. Finally, quasineutrality, which as shown in Ref. 1 is valid in the limit $\omega_{pi}^2 \gg \Omega_{ci}^2$, is used to close the system of equations. As in Ref. 1, finite gyroradius effects are ignored.

The constants of the motion for particles are the guiding center position,

$$X = x + v_y/\Omega_c; \tag{1}$$

the particle energy,

$$\epsilon = (1/2)mv^2 + q\phi(x); \tag{2}$$

and the component of the velocity parallel to the magnetic field,

$$v_z \quad . \tag{3}$$

Equilibria may then be specified using the constants of the motion to form model distribution functions for the ions and for the electrons.

The most basic distribution function is used for the electrons; that is a Maxwellian distribution in particle energy and a multiplicative factor depending upon the guiding center position. The model distribution function is therefore given by

$$F_e(X,\epsilon,v_z) = g_e(X) \exp\left[(-(1/2)mv^2 + e\phi(x))/T_e\right] \quad . \tag{4}$$

For the electrons finite gyroradius effects should be completely negligible. Therefore the equilibrium spatial distribution function for the electrons is given by

$$n_e(x) = N_e(x)\exp\left[e\phi(x)/T_e\right] \qquad (5)$$

where $N_e(x)$ may be arbitrarily specified.

The ions consist of two populations. One population is treated as a cold background. The second population consists of ions counter streaming along the magnetic field. The model distribution function for either population may be given by

$$F_i(X,\epsilon,v_z) = g_i(X)\exp(-\{\epsilon - 1/2mv_z^2 - \epsilon_0\}/T_1) \qquad (6)$$
$$\times \left\{exp[-.5(v_z-v_0)^2/v_{ti}^2]+exp[-.5(v_z+v_0)^2/v_{ti}^2]\right\}$$

where v_{ti} is the thermal velocity parallel to the magnetic field and T_1 is a parameter related to finite ion gyroradius. For the purposes of this paper ion gyroradius effects are ignored. Finite ion gyroradius effects are removed by taking the limit $T_1 \rightarrow 0$. At that limit the term $\exp(-\{\epsilon - 1/2mv_z^2 - \epsilon_0\}/T_1)$ reduces to a delta function at the minimum value for the perpendicular kinetic energy at the given value of x (which is the definition of ϵ_0). This minimum value of perpendicular kinetic energy corresponds to the $\mathbf{E}\times\mathbf{B}$ drift velocity due to any equilibrium electric field in the x direction.

Since finite gyroradius effects are being ignored, the guiding center variable X reduces to

$$X = x + v_y(x)/\Omega_{ci} \qquad (7)$$

where $v_y(x)$ is the $\mathbf{E}\times\mathbf{B}$ drift velocity and is a function of only the x coordinate. Therefore the spatial distribution function for the ions becomes

$$n_i(x) = N_i(x) \qquad (8)$$

where $N_i(x)$ is a completely arbitrary function and represents the total ion density including the background ions and the beam ions.

Quasineutrality then determines the equilibrium through the relation

$$N_e(x)\exp(e\phi(x)/T_e) = N_i(x) \quad . \qquad (9)$$

In addition, we may require that the equilibrium is field free, that is, the equilibrium electric field is zero everywhere. This requirement eliminates the free energy associated with the shear in the $\mathbf{E}\times\mathbf{B}$ velocity. In this paper linear theory will be performed only for model equilibria that are field free. However, some simulation work is included for the case where an equilibrium

electric field is present.

3. Linear Theory and Linear Simulation Results

Section 3A contains the linear theory for the inhomogeneous slab model of the previous section. Particle simulation techniques are used in order to recover linear behavior as described in Sec. 3B. The results obtained by linear theory are compared with the results obtained from the particle simulations.

3A. Linear Theory

The eigenmode equation for our problem can be obtained from the drift kinetic equation since $\omega \ll \Omega_{ci}$ and all finite gyroradius effects are being ignored. The drift kinetic equation is then linearized and Fourier transformed for a mode with finite values for both k_y and k_z. The resulting eigenmode equation is then easily obtained from Eq. (10-166) of Ref. 9 by summing over the background ion component and the ion beam component. Resonant electron effects, which are small corrections for this instability[1] , are ignored and only Debye shielding is retained for the electrons. The resulting eigenvalue equation is given by

$$A(x) \frac{\partial^2 \phi_{k_y\, k_z}}{\partial x^2} + B(x) \frac{\partial \phi_{k_y\, k_z}}{\partial x} - \Theta(k_y, k_z)\phi_{k_y\, k_z} = 0 \tag{10}$$

where

$$A(x) = \frac{\omega_{pi}^2}{k^2 \Omega_{ci}^2} \tag{11}$$

$$B(x) = (1 - 2\delta)\frac{\omega_{pi}^2}{k^2\Omega_{ci}^2}\frac{\partial \ln(N_c)}{\partial x} + 2\delta\frac{\omega_{pi}^2}{k^2\Omega_{ci}}\frac{\partial \ln(N_b)}{\partial x} \tag{12}$$

and $\Theta(k_y, k_z)$ represents the dispersion relation in the local approximation with $k_x = 0$ and is given by

$$\Theta(k_y, k_z) = \frac{\omega_{pi}^2 k_y^2}{k^2\Omega_{ci}^2} + (1 - 2\delta)\frac{\omega_{pi}^2 k_y \dfrac{\partial \ln(N_c)}{\partial x}}{\Omega_{ci}\omega k^2} \tag{13}$$

$$- \delta\frac{\omega_{pi}^2 k_y \dfrac{\partial \ln(N_b)}{\partial x}}{k^2 \Omega_{ci} k_z \sqrt{2}v_{ti}}\left\{ Z(\xi_+) + Z(\xi_-) \right\}$$

$$- (1 - 2\delta)\frac{\omega_{pi}^2 k_z^2}{k^2\omega^2} - 0.5\delta\frac{\omega_{pi}}{k^2 v_{ti}^2}\left\{ Z'(\xi_+) + Z'(\xi_-) \right\}$$

$$+ \frac{1}{k^2 \lambda_{De}^2}$$

Here ω_{pi} is the total ion plasma frequency, N_c is the cold background ion density, N_b is the total ion beam density, $\delta = N_b/(2N_c)$ represents the density of one ion beam, $k^2 = k_y^2 + k_z^2$, λ_{De} is the electron Debye length, Z is the usual plasma dispersion function, and $\xi_\pm = (\omega \pm k_z U_b)/(\sqrt{2} v_{ti})$ with U_b the average beam velocity along the magnetic field. The quantities ω_{pi}, N_c, N_b λ_{De} and δ are all functions of the x coordinate.

In order to solve Eq. (10) specific choices for the density profiles and boundary condition must be made. The intent of our calculations is only to include the dominant effects of the problem in the most straight forward manner possible. Therefore, for the calculations given in this paper, we choose the boundary conditions $d\phi/dx = 0$ at both boundaries. The ion density profiles are given the form

$$N_i(x) = n_0(1 + A\cos(\pi x/L_x)) \tag{14}$$

or

$$N_i(x) = n_0(1 + B\sin(\pi x/L_x)) \tag{15}$$

and may vary for the background ions and the beam ions. The electron density is then determined from quasineutrality; that is

$$N_e(x) = \sum_s N_i^{(s)}(x) \quad . \tag{16}$$

Equation 12 was solved by integrating the equation from both boundaries and matching the results in the center of the system. In this fashion it is possible to recover the family of complex eigenmodes $\{\phi_{k_y k_z}(x)\}$ and the corresponding eigenvalues $\{\omega\}$. For those cases where the local approximation is valid $k_y L_n \gg 1$ (where L_n is the background ion density scale length) the local approximation gives good agreement with the most unstable eigenvalue. However, in place of a single value for ω a set of eigenvalues is obtained. This fact makes it more difficult to isolate linear behavior in the simulation code, as will be discussed in Section 3B. For example, Fig. 2. shows the most unstable eigenmode and Fig. 3 shows the second most unstable eigenmodes for a test case with the parameters; $\omega_{max}^*/\Omega_{ci} = 0.03$, $k_y \rho_s = 0.74$, $k_z L_n = 0.16$, $U_b/c_s = 3.0$, $v_{ti}/U_b = 0.0$, and $\delta|_{L_x/2} = 0.1$. The wavevector was chosen so that

the growth rate is close to the maximum growth rate for the given physical parameters. Here c_s is the sound speed, $\rho_s = c_s/\Omega_{ci}$, L_n the the minimum value for the background ion scale length, and $\omega^*_{max} = c_s/2L_n$ represents the maximum drift wave frequency. The density profile from Eq. (14) is used with $A_b = -1.0$ and $A_c = 0.5$. The growth rates are very close to each other and therefore both may be expected to be present is simulations with random excitation.

The particular eigenmodes shown in Fig. 2 and Fig. 3 have their real and imaginary components almost equal. This fact means that the eigenmode has approximately elliptical potential contours in the plane of the electric field with one axis parallel to the x axis . This type of eigenmode structure is retained even when thermal effects are added.

Changing the beam ion density profile to that in Eq. (15) with the value $B_b = 1.0$ yields eigenmodes of a different nature as seen in Fig. 4. For this type of eigenmode the potential contours may be considered elliptical about the potential extrema but now neither axis is parallel to the x axis. Thus virtually any type of mode structure is possible for this problem.

Keeping k_y fixed and varying L_x causes the validity condition for the local approximation to be invalid and it is expected that $\gamma_{max}/\omega^*_{max}$ would decrease. This is indeed what happens. However, $\Omega_{ci}/\omega^*_{max} \approx k_y L_n$: therefore a decrease in L_x is leads to a larger growth rate. In this sense finite length effects do not serve to reduce the growth rate.

3B. Simulation Techniques and Linear Behavior

This section describes the simulation techniques and the linear phenomena recovered from the simulations. A quiet start technique is necessary to initialize the simulations and achieve good agreement with the theoretically calculated mode structures from the previous section.

The simulation code is a 2 - 1/2 dimensional electrostatic particle code with Boltzmann electrons. The field solve is quasineutrality as in Ref. 1. The geometry is that of Fig. 1 with the simulation plane at a small angle to the $x - y$ plane so as to include a finite value for the parallel wavevector k_z. The code employs periodic boundary conditions for the variation perpendicular to the x axis. The code reflects the particles at $x = 0$ and $x = L_x$. The electric field

component E_x is zero at $x = 0$ and $x = L_x$. Full ion dynamics are retained. This has the disadvantage of the introduction of ion cyclotron waves. However, since only the guiding center motion is important the time step does not have to accurately represent the high frequency waves present. Only a single beam will be unstable since only a single value of ω/k_z is possible using this $2 - 1/2$ dimensional model.

In order to recover the linear behavior with the nonlinear particle code numerical noise must be suppressed as much as possible in the choice of initial conditions. Therefore, for the purposes of comparing the code results with the results of linear theory we choose a case where the initial thermal spread in v_z is zero. In addition, the particles were loaded in a with very special initial conditions. For the equilibrium the particles were loaded uniformly in both the x direction and in the y direction. This uniform loading guarantees equivalent particle statistics at each location in the simulation. In order to represent the density gradient it is necessary to weight the particles according to the exact value of the density at the position they are loaded.

These techniques are , in general, not enough. As was mentioned in the previous section the generic equilibrium has many closely-spaced eigenvalues. Even with the low noise level in the equilibrium the most unstable mode will not be able to become dominant before the simulation becomes nonlinear. Therefore special initial perturbations are required.

One approach is to integrate the particles in the fields of the most unstable waves. This may be done either numerically or analytically. When this was done either way the self consistent field as computed from the particles was very close to the theoretical field. This does suggest that the calculated solutions are indeed self-consistent solutions.

By using this type of initial condition the simulation can then be carried out in a self-consistent manner. Items of interest include the real frequency, the growth rate, and the mode structure in the inhomogeneous x direction. The physical parameters are those of Fig. 2 and Fig. 3. The simulation parameters are $\Omega_{ci}\Delta t = 0.5 - 1.0$, the number of grids in the x direction is $N_x = 65$, the number of grids in the periodic direction is 32, and roughly six thousand particles for the background ions and sixteen thousand particles for each of the beams. Larger

time steps can be taken by use of a first order particle integration scheme to remove the time constraint caused by the high frequency waves[10]. In addition, only one mode was kept in the periodic direction and only eight modes were kept in the inhomogeneous x direction. The equilibrium has no initial electric field.

Figure 5 shows the the potential as a function of time for a location near the center of the mode structure. Notice that due to the approximate normal mode initialization the perturbation begins growing with a definite frequency almost immediately; i. e. there is only a small component present that does not comprise part of the normal mode. The real frequency and growth rate are within about 5% of the numerically calculated values. Figure 6 shows the recovered eigenmode from the simulation during the linear stage using the Zed analysis package[11].

The results given in Fig. 5 and Fig. 6 are good. However, the agreement is certainly not exact. Sources of discrepancy include (1) retaining only the low frequency response (i.e. ignoring terms of order $\omega/\Omega_{ci} \simeq 0.025$), (2) not including all of the Fourier components necessary for complete representation of the mode structure (3) the excitation of cyclotron modes and (4) the excitation of secondary normal modes due to the sensitivity of the initial excitation. These last three effects will now be discused individually.

Fourier decomposition of the calculated mode structures allows one to determine how many modes to keep in the simulations. Unfortunately the mode structures typically have a tail of a few percent at wavelengths of 10 - 15 times the primary wavelength.

These shorter wavelengths give high cyclotron noise unless large numbers of particles are being used to represent the ion beams. This noise is due primarily from the extra degree of freedom in ion phase space associated with the gyromotion. Thus the particle motion need not (and in general does not) contain just the low frequency drift motion. Since $\omega \ll \Omega_{ci}$ the high frequency ion cyclotron waves may randomize portions of the particle phase space during an e-folding time of the instability.

The initial excitation requires accurate knowledge of the real frequency and the growth rate. Deviation from the true values yields phase errors between the perturbed positions and velocities. This then excites other normal modes with a finite amplitude. Some of these other normal modes have comparable real frequencies and growth rates, which makes interpretation of simulation results more difficult.

4. Nonlinear Behavior

This section describes the dominant nonlinear effects as observed in the simulations. These effects include (1) $E \times B$ trapping of resonant beam ions, (2) modification of the density profiles of the different species, and (3) weakly nonlinear electrons.

4A. Nonlinear Effects

Some of these effects were discussed in an earlier paper[1] and the results are summarized in Table 1. These results were obtained by assuming a local approximation for the fields, that is, that the perturbation electric field is assumed to be zero in the x direction.

We wish to review some of the analysis for the case of a single wave $\phi = \phi_0 \cos(k_y y + k_z z)$ in the local approximation; i.e. there is no x dependence in the problem. The approximate scaling law for saturation by particle trapping in the local approximation is given by

$$\frac{e\delta\phi}{T_e} \approx \frac{\gamma^2}{k_z^2 c_s^2} 3$$ (17)

which is obtained by equating the linear growth rate of the instability γ to the trapping frequency of the particle in the wave field given by $k_z \sqrt{e\delta\phi/m}$. (The factor 3 represents an "e-folding" from the onset of nonlinear effects to saturation and is very qualitative in nature) Associated with the trapping in v_z is displacement in the x direction governed by the relation

$$v_z - \left[k_z/k_y\right]\Omega_{ci} x = \text{constant} \quad .$$ (18)

Equation (18) is obtained by using the guiding center equations of motion. Equation (18) implies that trapped particle are transported in x. The signs of the various quantities in Eq. (18) are such that the trapped ions (particles that lose energy on the average) have a net drift up the background ion density gradient.

One of the goals of this paper is to relax the local approximation. The analysis and simulations will be limited to the case of a single value for (k_y, k_z). As mentioned before, only one ion beam will be unstable since only one value for ω/k_z is allowed in the simulation model. An important change in the nonlocal problem over the local problem is that the local treatment assumes that there is no perturbed electric field parallel to the density gradient. Particle orbits are constrained so that their $\mathbf{E}\times\mathbf{B}$ drift velocity perpendicular to the density gradient is zero. Inclusion of the correct electric field means that particles may have a component of their drift velocity perpendicular to the density gradient. A second important feature is that simulations using the local approximation employ density profiles that do not change (since the electric fields are independent of the x coordinate). This is not true for nonlocal simulation models.

One interesting fact is that the constant of motion given in Eq. (18) is unchanged even for the nonlocal problem as long as there is only a single value for the wavevector (k_y, k_z); that is, the potential has the form

$$\phi(x,y,z,t) = \phi_0(x,t)\cos(k_y y + k_z z - \omega t) \tag{19}$$

and the time variation of the potential satisfies $\partial/\partial t \ll \Omega_{ci}$ so that the guiding center approximation may be made. The polarization drift velocity is very small compared to the $\mathbf{E}\times\mathbf{B}$ drift velocity and is therefore neglected in the derivation of Eq. (18).

As mentioned above, one effect missing entirely in the local approximation is the effect of electric field parallel to the density gradient. This may cause $\mathbf{E}\times\mathbf{B}$ trapping. Idealizing the problem to the case where the electric field is entirely perpendicular to the magnetic field allows a clear intuitive picture of $\mathbf{E}\times\mathbf{B}$ trapping. Consider a resonant particle moving in the plane perpendicular to the magnetic field and retain only the $\mathbf{E}\times\mathbf{B}$ drift velocity. The particle attempts to stay on equal potential contours and to drift around them. If the particle may drift around the potential contours and change its position significantly (comparable to the scale lengths of the problem) , then linear theory is no longer valid.

An estimate for when $\mathbf{E}\times\mathbf{B}$ trapping is important can be obtained from equating the wave frequency in the particle frame with the frequency for a particle to drift around one of the

potential peaks. This yields

$$\omega' = \omega_{E \times B} \tag{20}$$

with

$$\omega_{E \times B} \approx (k_x k_y) \left| \frac{e\phi}{T_e} \right| c_s^2 / \Omega_{ci} \tag{21}$$

where ω' is the wave frequency in the particle frame. The condition for importance of this effect is then given by

$$\left(\frac{k_y c_s}{\Omega_{ci}} \right) k_x c_s \left| \frac{e\phi}{T_e} \right| \approx \omega' \tag{22}$$

The analysis is actually far more complicated than is suggested above. The reason is that the wave has a nonzero electric field component in all three important directions in this problem. The effects of the constant of the motion given in Eq. (18) must be combined with the motion produced by E_x in determining actual particle orbits. Equation (18) implies that particles with circular type motion in the $x - y$ plane have their v_z changing in a like manner. The particle orbits are actually very problem dependent since the orbits depend on the phase structure of the eigenmodes. The phase structure of the eigenmode can vary greatly, as shown in Sec. 2A.

4B. Simulation Results

Nonlinear phenomena recovered from the simulations are presented in this section. Connections will be made to the nonlinear phenomena discussed in the previous section; (1) $\mathbf{E} \times \mathbf{B}$ trapping, (2) the final appearance of the density profiles and (3) saturation levels. An exhaustive parameter search is entirely out of the question. Parameters that will be varied are (1) the thermal spread of the beams, (2) the density profile of the ion beams and (3) whether the equilibrium has a zero order electric field.

One set of simulations was performed in order to investigate the effects of the thermal spread along the magnetic field on the saturation of the instability. The physical parameters are those corresponding to Fig. 2. and Fig. 3 except that $A_b = 0.0$. The simulation parameters are $\Omega_{ci} \Delta t = 0.5$, $N_x = 65$ grids in the x direction and 32 grids in the periodic direction and roughly

thirty thousand particles. The values for the length in the periodic direction was chosen so that (k_y, k_z) corresponded to the values for the most unstable root in the local approximation. Eight modes were kept in the inhomogeneous direction. The thermal spread was varied from $v_{ti}/U_b = 0.0$ to $v_{ti}/U_b = 0.25$. These were the same simulation parameters used for previous simulations using the local approximation[1]. Typically many orders of magnitude in growth in the mode energy was observed in the simulations as shown in Fig. 7.

The saturation values are shown in Table 2 for the simulations. As can be seen the saturation level is relatively independent of the beam thermal spread parallel to the magnetic field unlike the simulation in Ref. 1. This result is very suggestive of $\mathbf{E} \times \mathbf{B}$ trapping as opposed to trapping in the direction parallel to the magnetic field since the saturation lelel does not depend much on the growth rate, in conflict to Eq. (17). Had both beams been unstable (which would require a fully three dimensional simulation code) then one would expect that the peak potential energies would be on the order of 20% of the electron thermal energy.

The estimate for when a resonant particle would become nonlinearly dominated by the motion perpendicular to the magnetic field is approximately when the $\mathbf{E} \times \mathbf{B}$ trapping frequency is comparable to the residual wave frequency induced by parallel trapping. Expressing this in terms of an approximation yields

$$k_y \rho_s k_x \left[e\phi/T_e \right] \approx k_z \left[e\phi/T_e \right]^{1/2} \tag{23}$$

or rewritten as

$$e\phi/T_e \approx \left(\frac{k_z}{k_x} \right)^2 \left(\frac{1}{k_y \rho_s} \right)^2 \quad . \tag{24}$$

This saturation level is approximately independent of the growth rate for this mechanism, although a slight dependence still exists because the percent of resonant particles plays a role in determination of the final saturated potential.

More evidence for the saturation mechanism may be presented by a careful examination of test particle orbits. In particular particle trajectories in the plane perpendicular to the magnetic fields are informative. A test particle trajectory for one simulation is shown in Fig. 8.

Notice that the orbit is consistent with E×B trapping; that is particle motion in both directions perpendicular to the magnetic field is significant. Figure 9 shows the potential as a function of space near saturation of the instability.

Particle trajectories may have a different appearance the trajectory shown in Fig. 8. Figure 10 gives another example of E×B trapping for a different situation. Notice that the particle motion in both directions perpendicular to the magnetic field is significant although the exact particle motion is quite different from that in Fig. 9. The particle motion depends upon how close that particle is to resonance with the wave and upon the spatial mode structure of the wave. Also, even with a single value for $\{k_y, k_z\}$, several eigenmodes may be present. Thus the exact motion is very complicated in general.

In order to examine the constant of motion given by Eq. (19) a group of test particles with the same initial values of x and v_z was followed. Constancy of the entity in Eq. (18) implies that the particles should fall on a line in $x - v_z$ plane. This was tried and proved to be a useful diagnostic as presented in Fig. 11. Notice that particles that lost energy suffered displacements up the background ion density gradient. Since more ion beam particles lose energy than gain energy a net displacement should occur in the ion beam density profiles. This characteristic is seen in Fig. 12.

The displacement of the ion beam need not be small. To examine this a very unstable case is chosen with $A_b = -1.0$, $v_{ti}/U_b = 0.19$ and the other parameters the same as the previous simulations. This type of ion beam density profile is an idealization of the situation that may occur when the injected neutral beam does not penetrate far into the plasma. Figure 13 displays the changes in the density profiles occurring for the simulation. The situation may be clarified further by examination of the particle distribution functions over different portions of the simulation region. Those regions that suffered a net density decrease did so at the expense of the lower energy beam ions. Those particles were transported up the background ion density gradient. These considerations are seen in Fig. 14.

Finally, a short discussion is included on the effects caused by an equilibrium electric

field. First consider the case of a uniform electric field in the x direction. Formal substitution into the local or nonlocal dispersion relation shows that the growth rates and wavevectors do not change. However, the real frequencies become

$$\omega_{\pm} \approx \pm k_z U_b - k_y V_E \tag{25}$$

where $V_E = E_0/B$ is the zero order drift velocity in the y direction. For typical parameters of this problem $k_y V_E$ is not negligible to $k_z U_b$. For the case where the electric field is pointing toward the walls, the signs of the quantities in Eq. (25) are such as to decrease the magnitude of the frequency in the laboratory frame. In the extreme limit, this effect may cause the perpendicular phase velocity to be in the ion diamagnetic drift velocity rather than in the electron diamagnetic drift direction.

When V_E is spatially dependent the situation is quite different. The phase velocity of the wave in the frame of the background plasma then depends upon the location in x. Therefore, in principle, any portion of the distribution function may be in resonance. In addition, one might expect that spatial dependence of equilibrium quantities such as the electron temperature the magnetic field and the zero order electric field would cause the saturation to be more mild. Simulation results tend to support this idea. An example is shown in Fig. 15 which shows the change in the linear frequency. Figure 16 shows the density profiles at saturation.

5. Conclusions

In this paper both linear and nonlinear properties of an ion-beam driven drift instability are described using an inhomogeneous slab model. The agreement between linear theory and the simulation model is modestly good. The linear effects of some of the parameters are discussed. In addition, the particle simulations give insight into the nonlinear saturation of the instability. The most relevant nonlinear effects for present experiments are (1) E×B trapping of the beam ions, (2) cross field transport of the trapped beam ions and (3) weakly nonlinear electrons. It is interesting to note that the beam ions are, on average, transported up the background ion density gradient. This fact suggests that the instability presented here may actually serve to improve confinement of the high energy beam ions.

Acknowledgements

References

1. V. A. Thomas and W. M. Nevins, Submitted for publication.

2. W. W. Lee and H. Okuda, Phys. Rev. Lett. **36** , 870 (1976).

3. C. Z. Cheng and H. Okuda, Phys. Rev. Lett. **38** , 708 (1977).

4. W. W. Lee and H. Okuda, J. Comp. Phys. **26** , 139 (1978).

5. B. I. Cohen, N. Maron, and G. R. Smith, Phys. Fluids **25** , 821 (1982).

6. W. W. Lee, Phys. Fluids **26** , 556 (1983).

7. Yu-Jiuan Chen, W. M. Nevins, and C. K. Birdsall, Phys. Fluids **26** , 2501 (1983).

8. J. F. Drake and J. D. Huba, Phys. Fluids **25** , 1207 (1982).

9. G. Schmidt, *The Physics of High Temperature Plasmas* , Academic Press, New York, NY. (1979).

D. C. Barnes, T. Kamimura, J.-N. Leboeuf, and T. Tajima, J. Comp. Phys. **52** , 480 (1983).

11. W. M. Nevins, private communication.

	v_{ti}/U_b	
δ	**small**	**large**
weak	ion beam trapping; enhanced cross-field motion of trapped ions; coherent mode coupling	trapping of resonant ions; enhanced cross-field motion of trapped ions
strong	nonlinear electrons; non-linear motion parallel to the density gradient; ion beam trapping; enhanced cross field motion of trapped beam ions	trapping of resonant ions; enhanced cross-field motion of trapped ions; weakly nonlinear electrons

Saturation Characteristics

TABLE 1. Nonlinear properties as a function of parameter space.

Saturation Dependence of Thermal Spread					
v_{ti}/U_b	0.00	0.07	0.13	0.19	0.25
$\gamma_{max}/\omega^*_{max}$	0.15	0.13	0.11	0.078	0.053
$(e\delta\phi/T_e)_{sat.}$	0.12	0.12	0.11	0.10	0.082

TABLE 2. Variation of saturation with the parallel thermal spread of the ion beams. The very weak dependence of the saturation on the growth rate suggests $E\times B$ trapping.
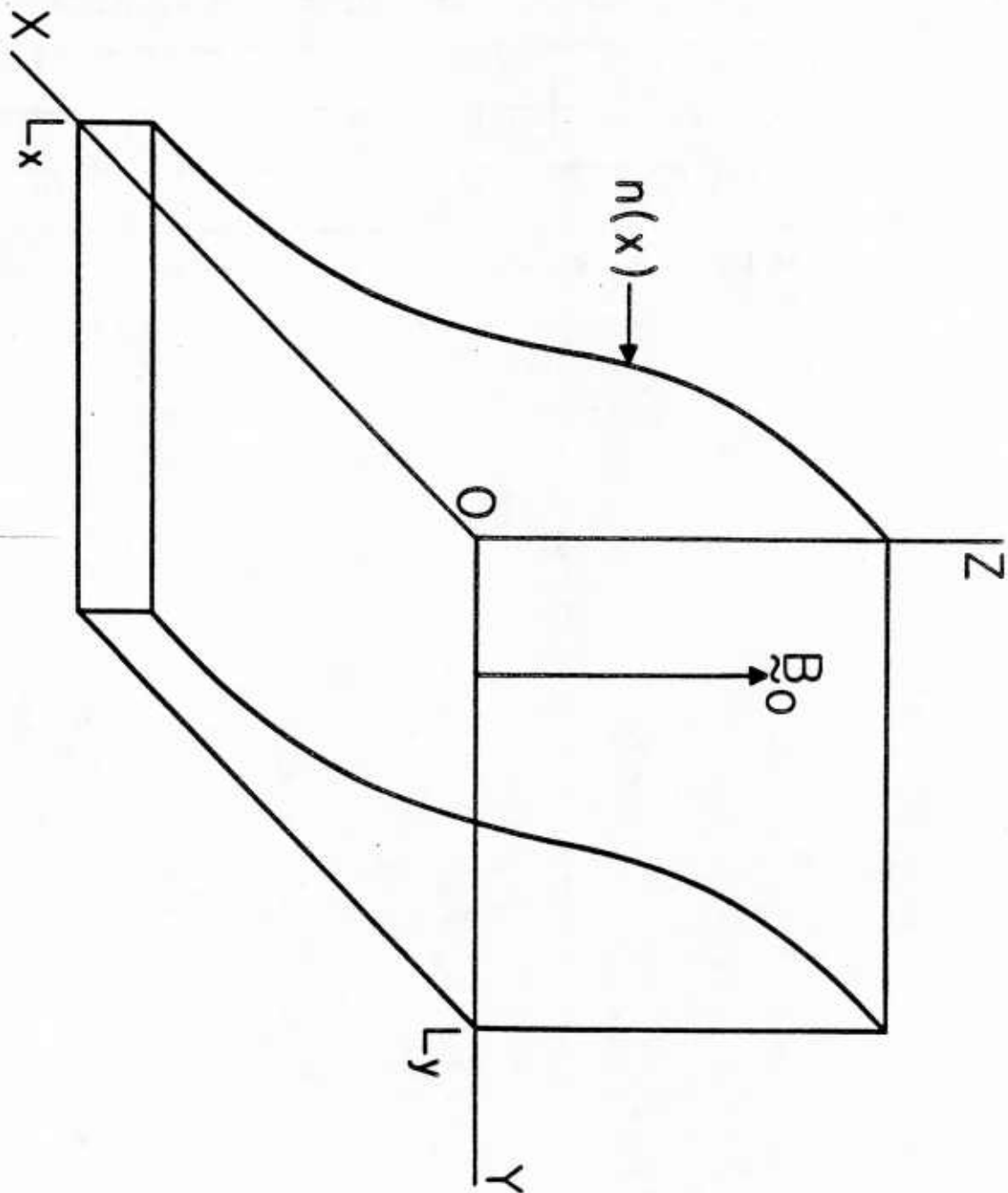
FIG. 1. Slab geometry for the instability. The magnetic field is uniform in space.

$$\phi_{k_y, k_z}(x)$$
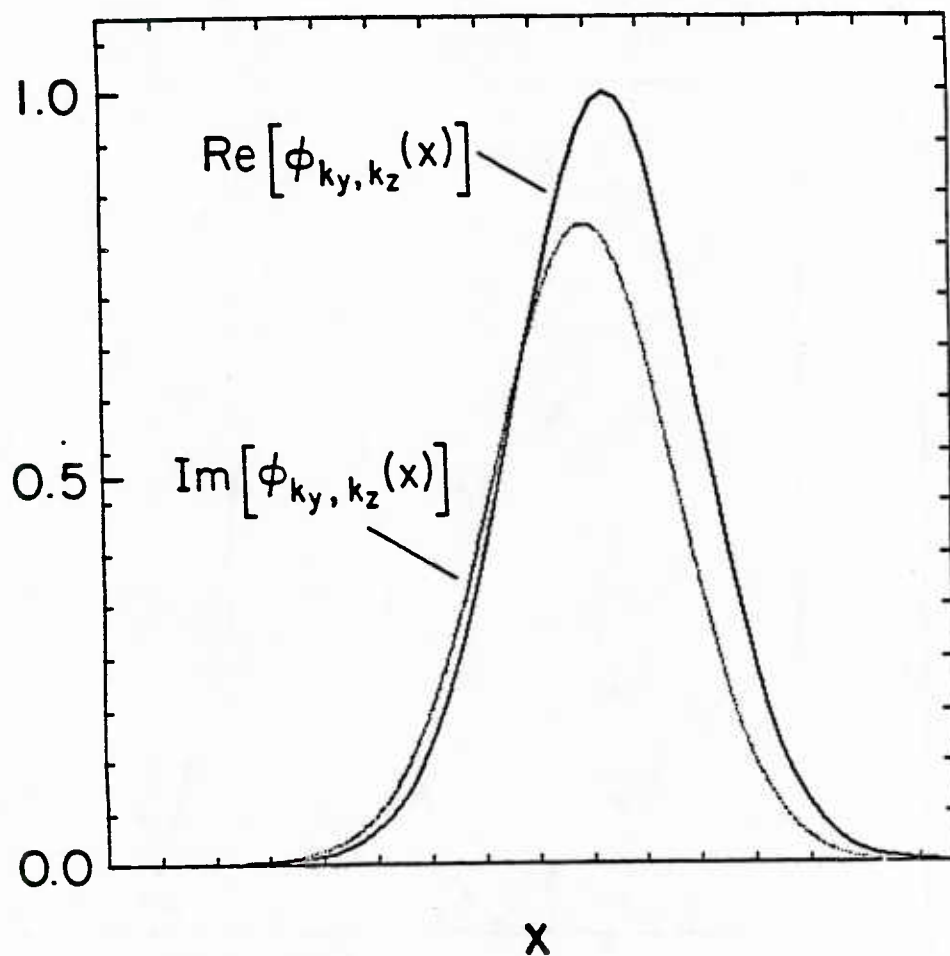
FIG. 2. Numerically obtained solutions to the eigenvalue problem for the most unstable solution showing (a) real and imaginary parts and (b) the square of the amplitude. The complex frequency is given by $\omega_r/\omega_{max} = 0.78$ and $\gamma/\omega_{max} = 0.28$.

$$\left| \phi_{k_y, k_z}(x) \right|^2$$

X

FIG. 2b.

$$\phi_{k_y,\,k_z}(x)$$

1.0

$Im\left[\phi_{k_y,k_z}(x)\right]$

$Re\left[\phi_{k_y,k_z}(x)\right]$

0.0

-1.0
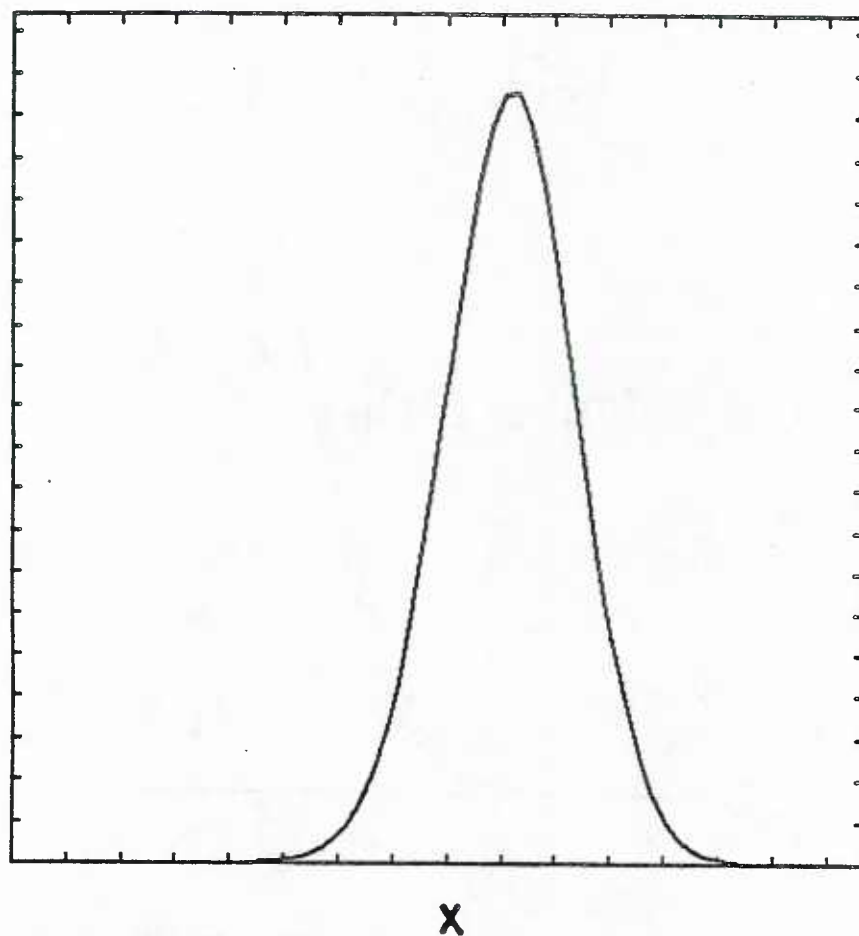
X
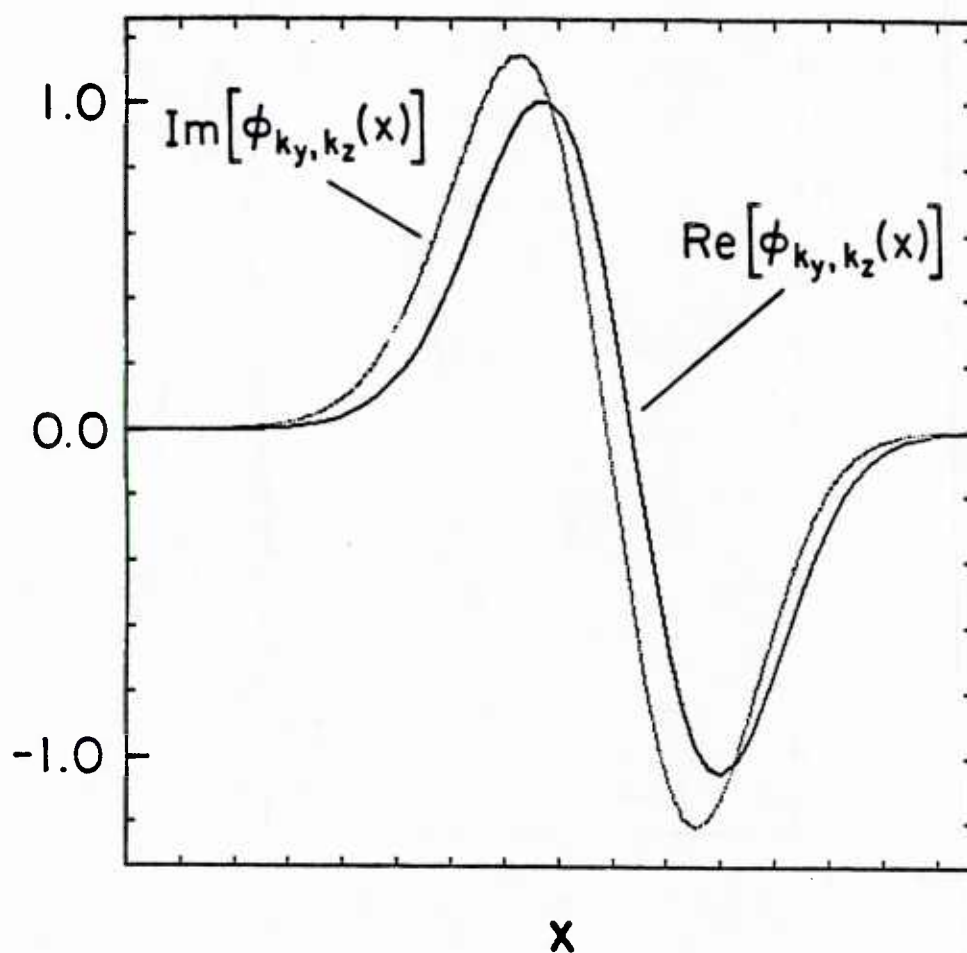
FIG. 3. Numerically obtained solutions for the second most unstable solution showing (a) the real and imaginary parts and (b) the square of the amplitude. The complex frequency is given by $\omega_r/\omega_{max}^{\bullet} = 0.74$ and $\gamma/\omega_{max}^{\bullet} = 0.25$.

$$\left|\phi_{k_y, k_z}(x)\right|^2$$
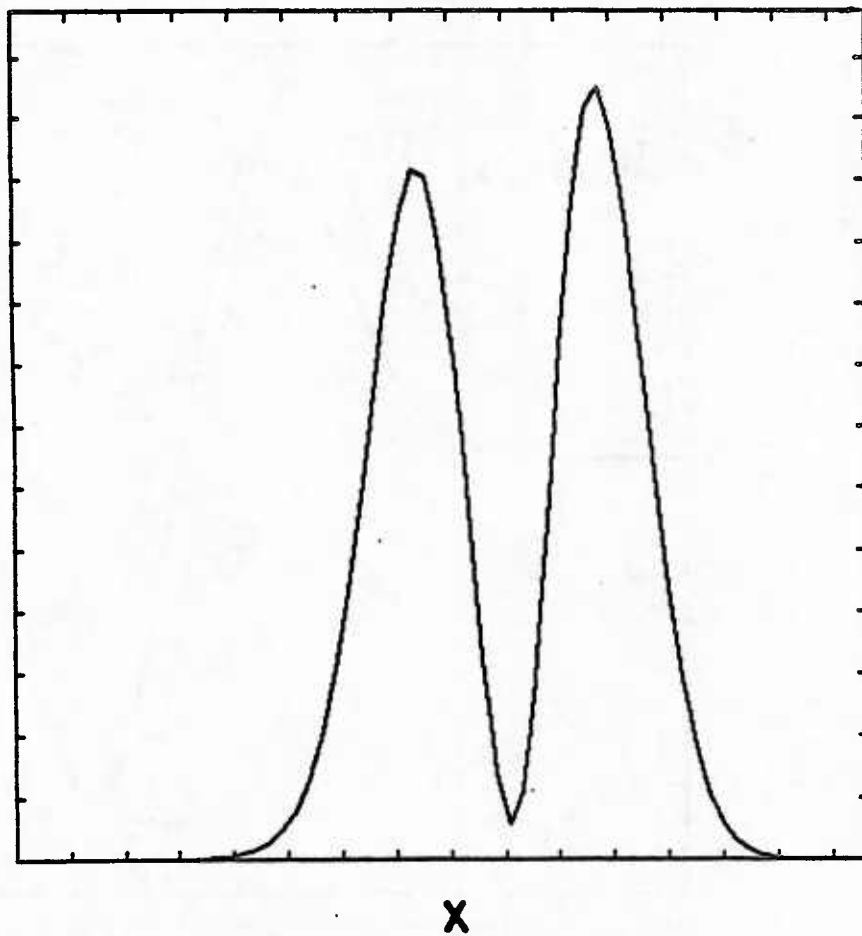
FIG. 3b.
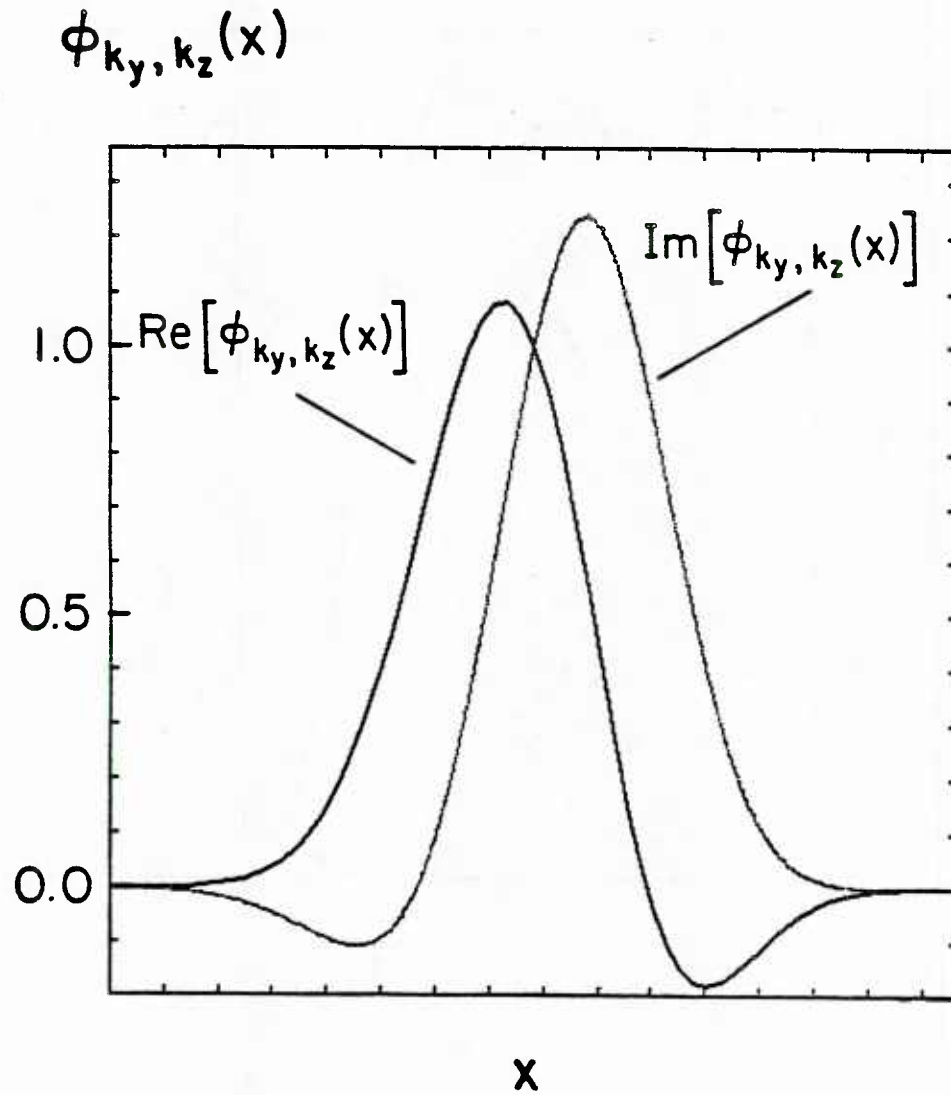
FIG. 4. Numerically obtained solutions using the beam ion density profile from Eq. (15) showing the real and imaginary parts for (a) the most unstable mode and (b) the second most unstable mode. The complex frequencies are $\omega_r/\omega_{max}^{\cdot} = 0.77$, $\gamma/\omega_{max}^{\cdot} = 0.098$ and $\omega_r/\omega_{max}^{\cdot} = 0.75$, $\gamma/\omega_{max}^{\cdot} = 0.081$ respectively. The growth rates are separated more than for the previous case considered, presumably because the spatial variation in the equilibrium is larger.

$$\phi_{k_y, k_z}(x)$$
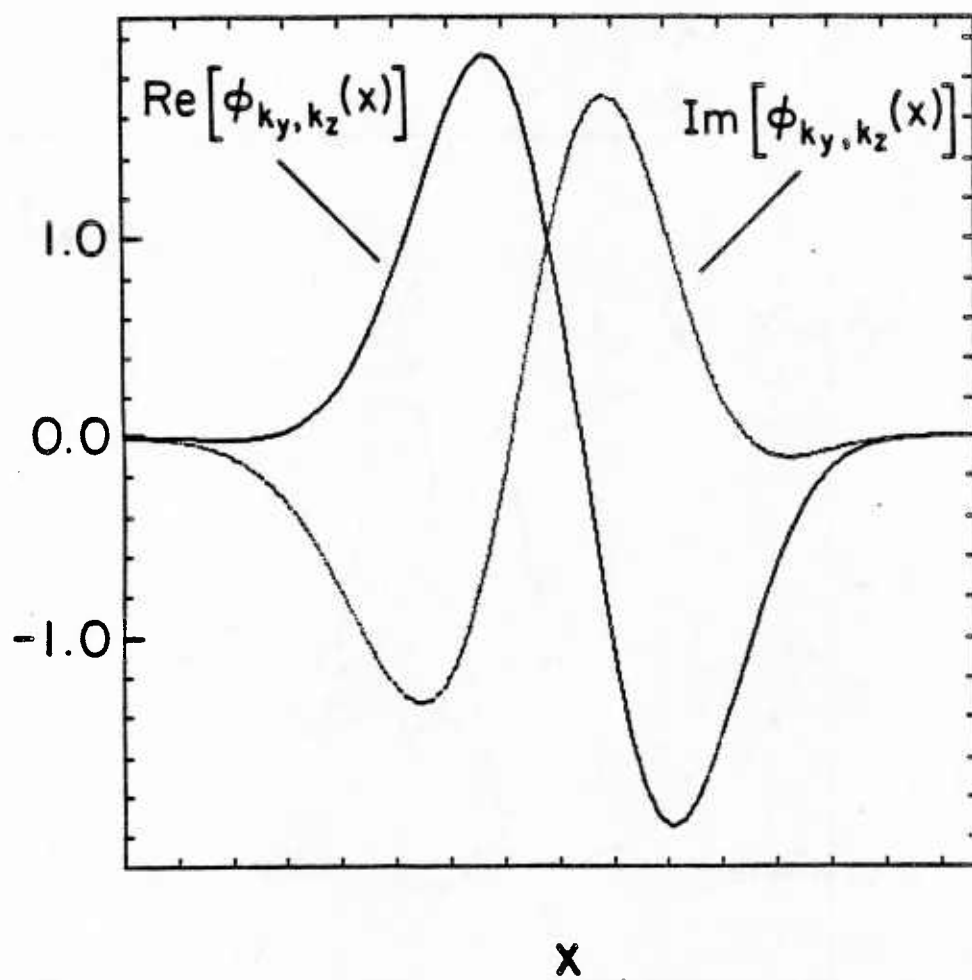
FIG. 4b.

$$\mathrm{Re}\!\left[\phi_{k_y,\,k_z}(x_0)\right]^2$$
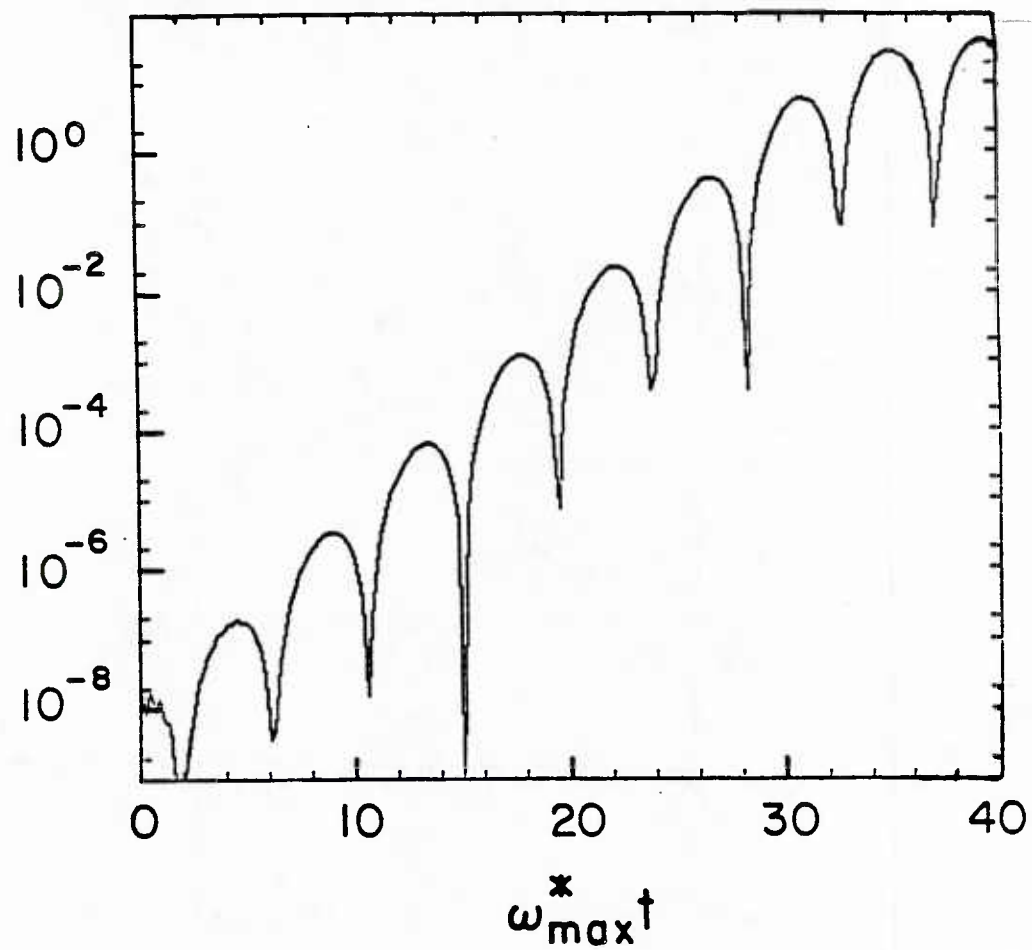
FIG. 5. Time history of (a) the square of the real component and (b) the square of the total perturbed potential for a fixed location x_0.

$$\left|\phi_{k_y, k_z}(x_0)\right|^2$$
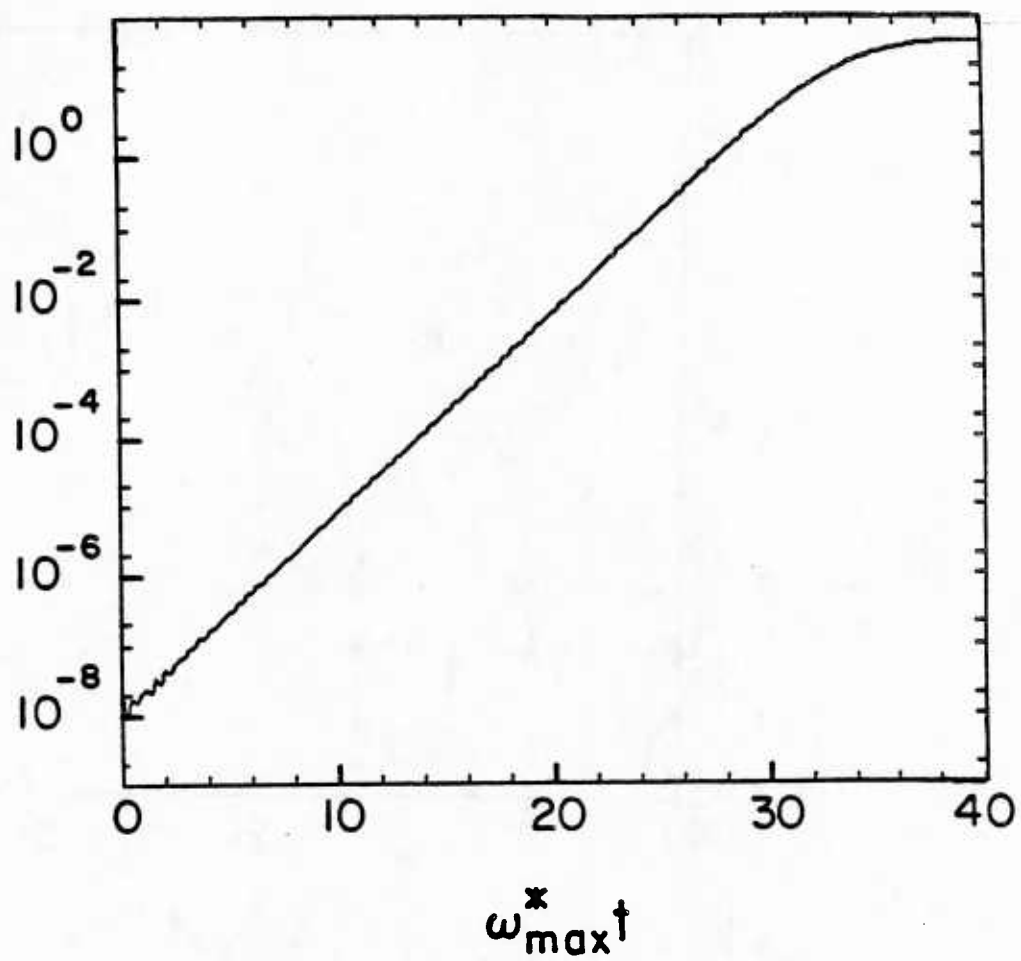
FIG. 5b.

$$\phi_{k_y, k_z}(x)$$
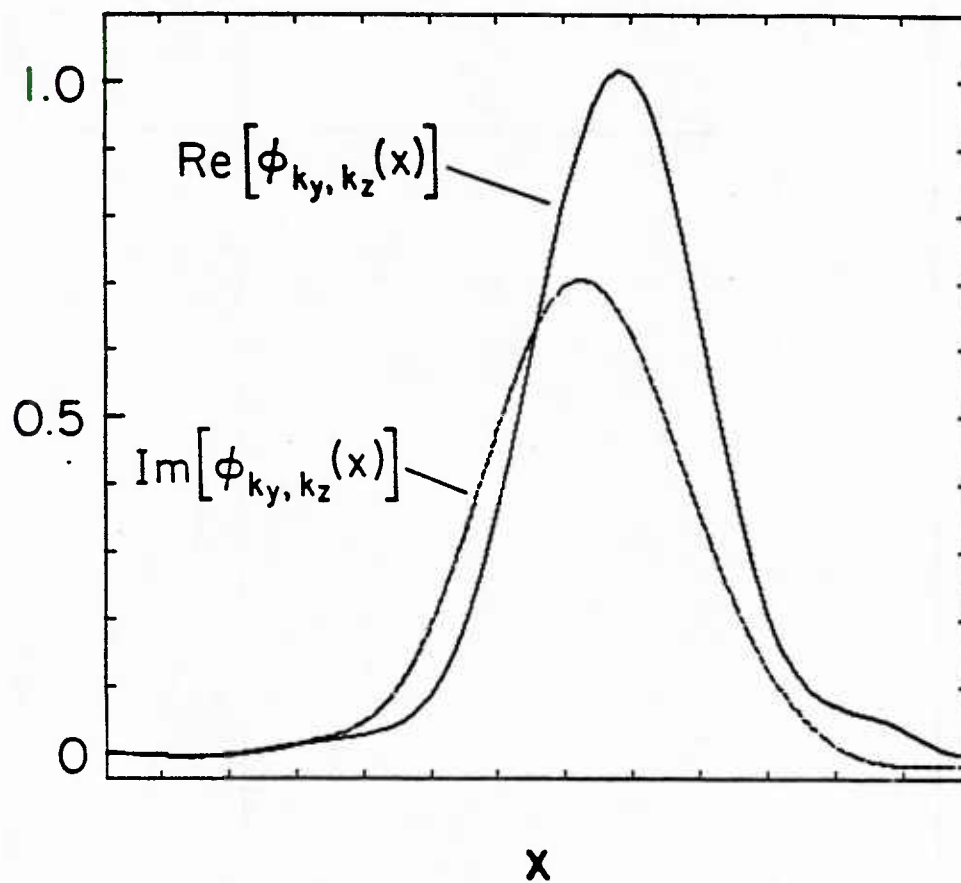
FIG. 6. Mode structures obtained from simulations showing (a) the real and imaginary parts and (b) the square of the mode amplitude as functions of the x coordinate.

$$\left|\phi_{k_y,\,k_z}(x)\right|^2$$
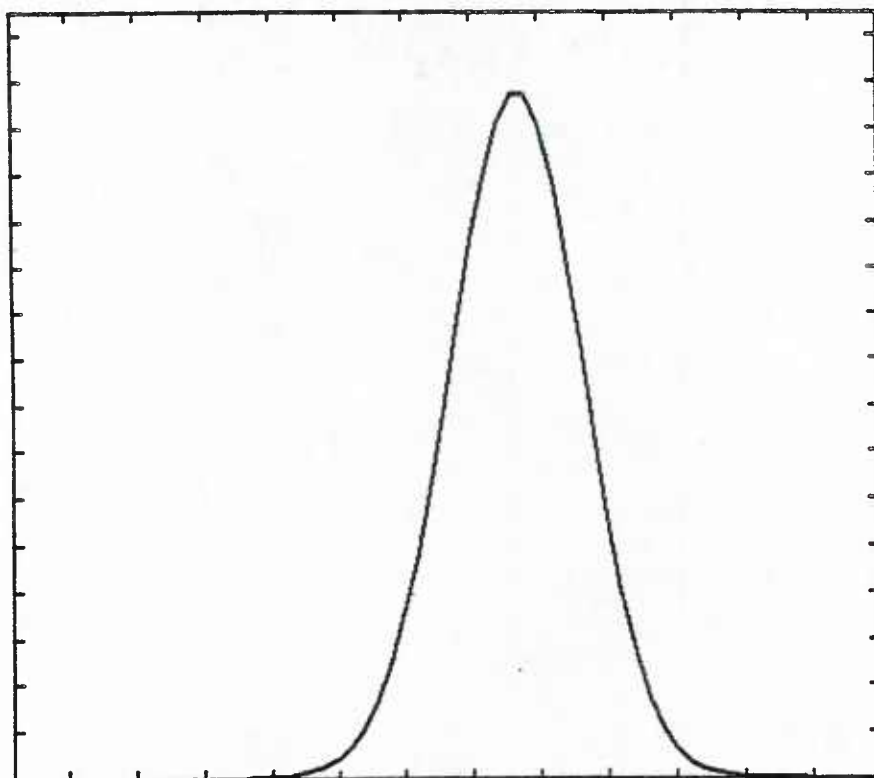
FIG. 6b.

$$Re\left[\phi_{k_y,k_z}(x_0)\right]^2$$
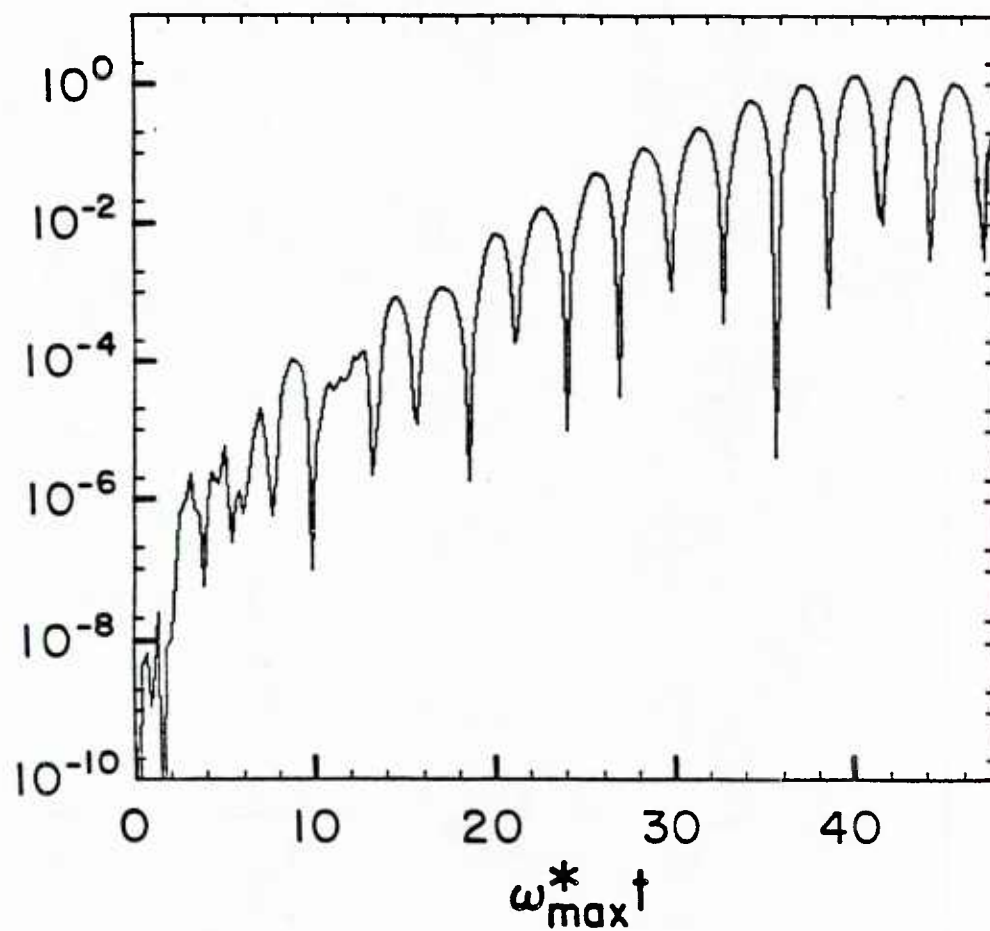
FIG. 7. Time history of the square of the real part of the potential at a fixed location x_0 as a function of time for the case $v_{ti}/U_b = 0.13$.
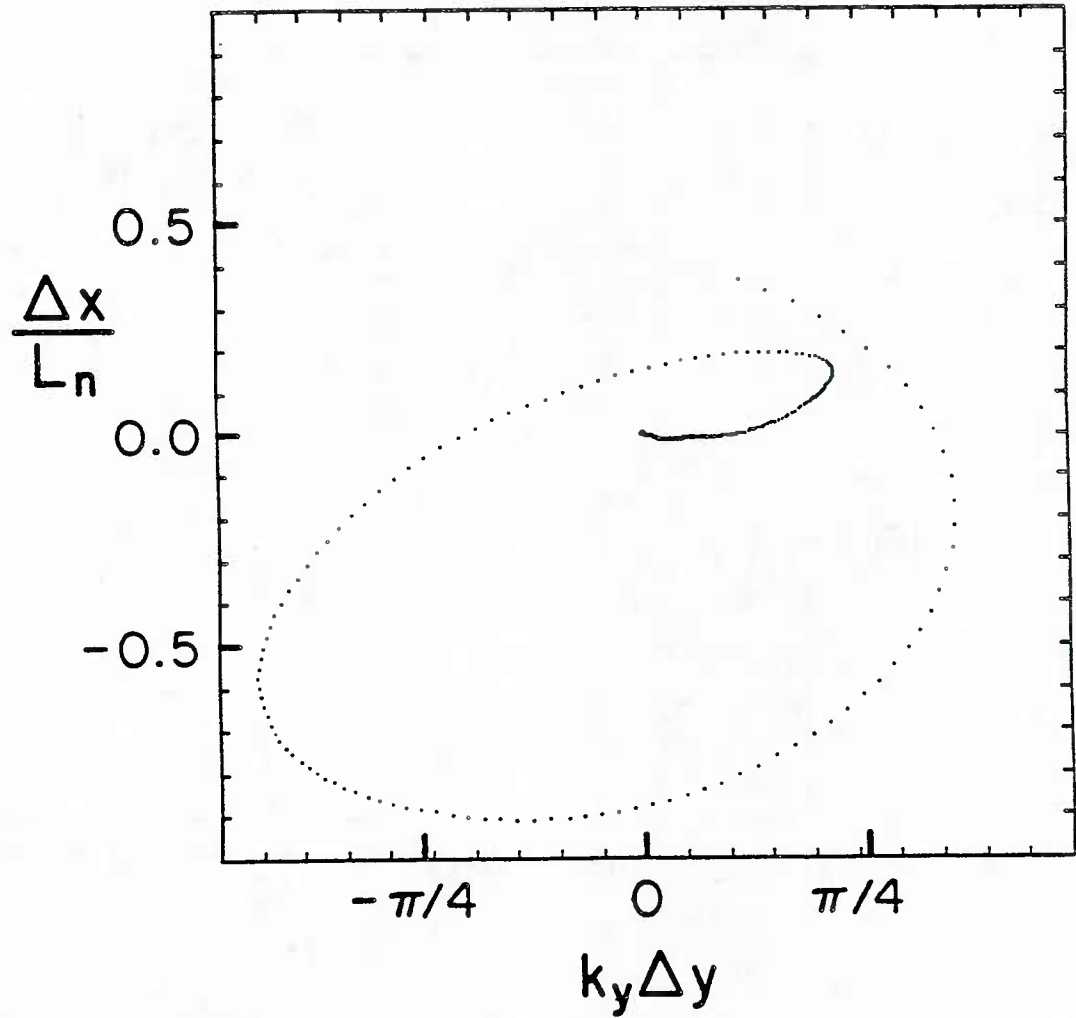
FIG. 8. Test particle time history in the $k_y\Delta y - \Delta x/L_n$ plane showing the spiral orbits. Initially the particle was in the center of the simulation region. This is from the simulation with $v_{\parallel}/U_b = 0.13$. The test particle initially had a parallel velocity slightly larger than the parallel phase velocity of the wave.
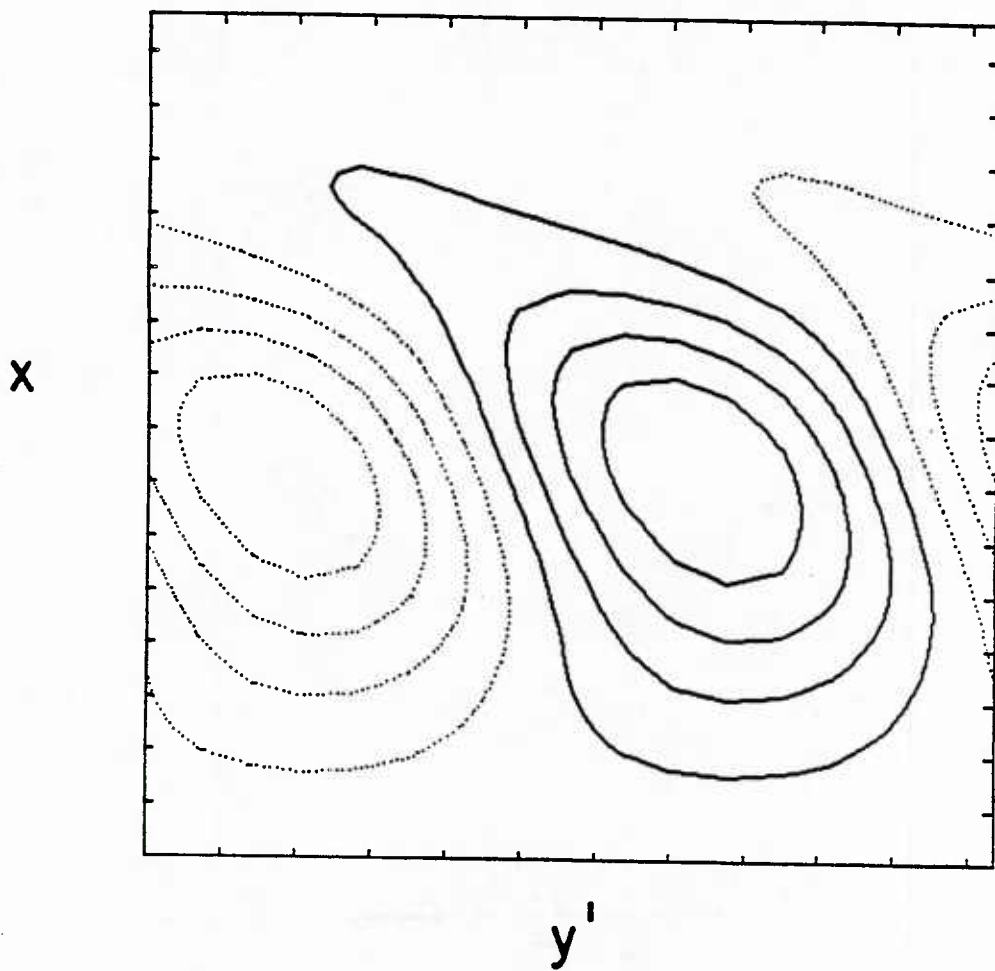
FIG. 9. Spatial structure of the potential at saturation for the simulation of FIG. 7 - 8. The contours are equally spaced with the dotted lines indicating a negative value and the solid line indicating a positive value.
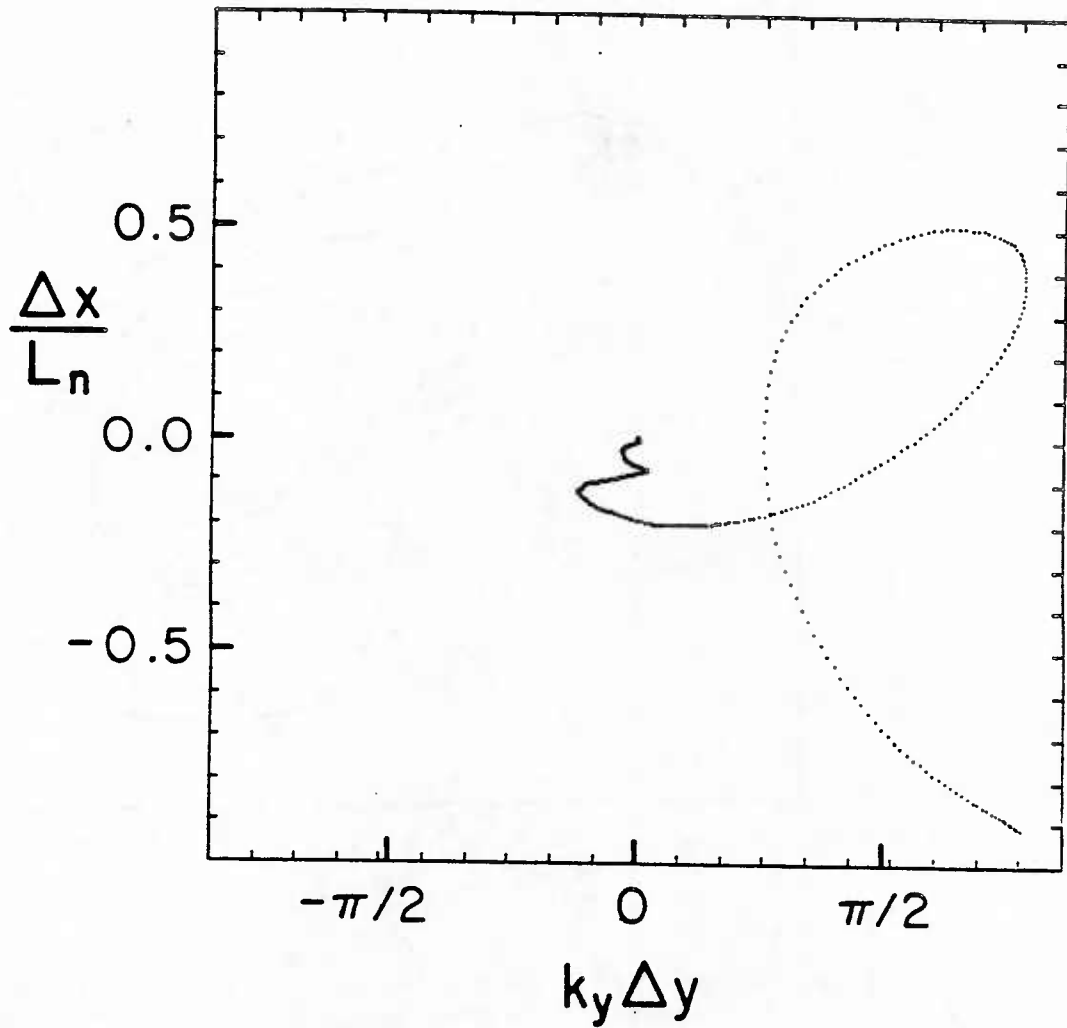
FIG. 10. Test particle time history in the $k_y \Delta y - \Delta x / L_n$ plane showing the spiral orbits. Initially the particle was in the center of the simulation region. This is from the simulation with $v_{//} / U_b = 0.25$. The test particle initially had a parallel velocity slightly larger than the parallel phase velocity of the wave.
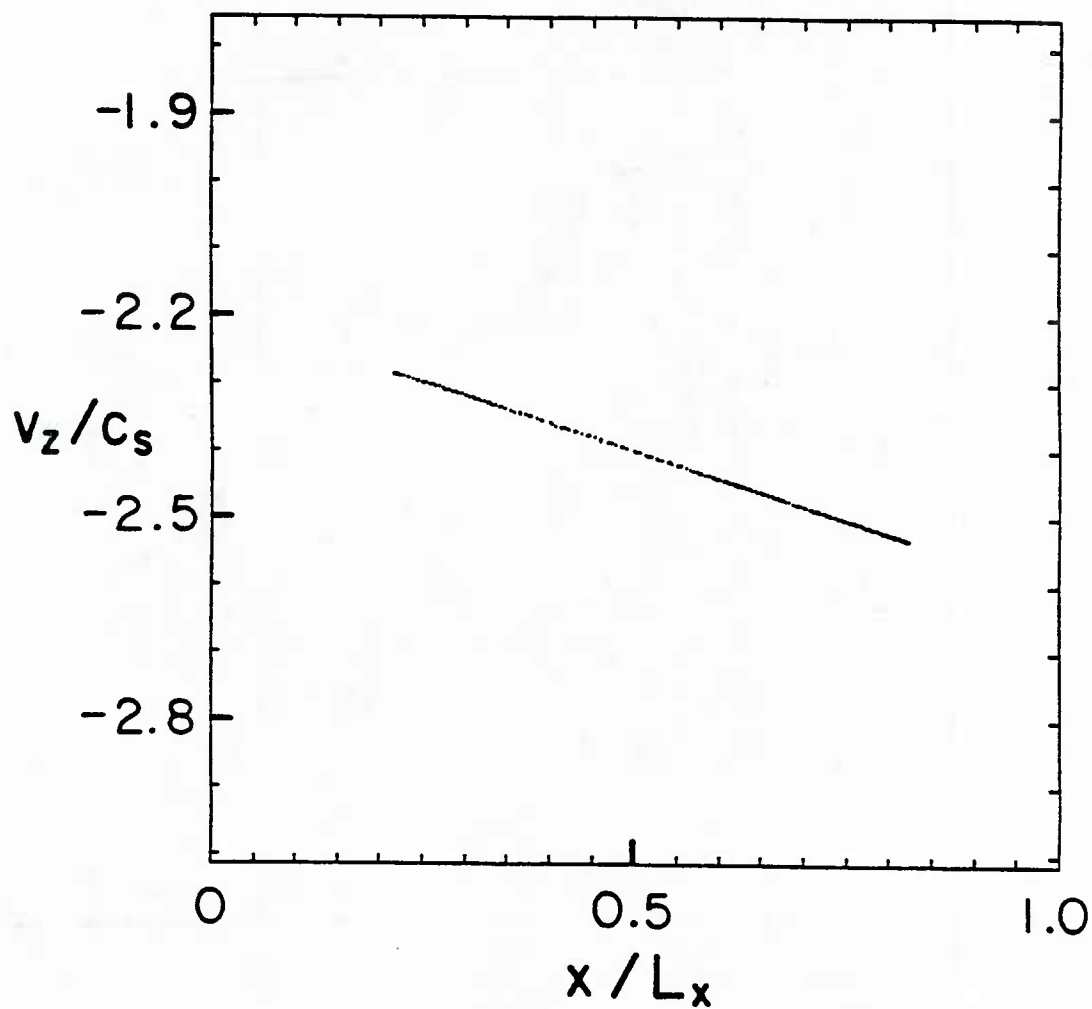
FIG. 11. Test particle motion in the $x - v_z$ plane at saturation of the instability for the case $v_{ti}/U_b = 0.19$. Here all of the particles had initial x locations in the center of the system. Their periodic dimension was loaded uniformly.
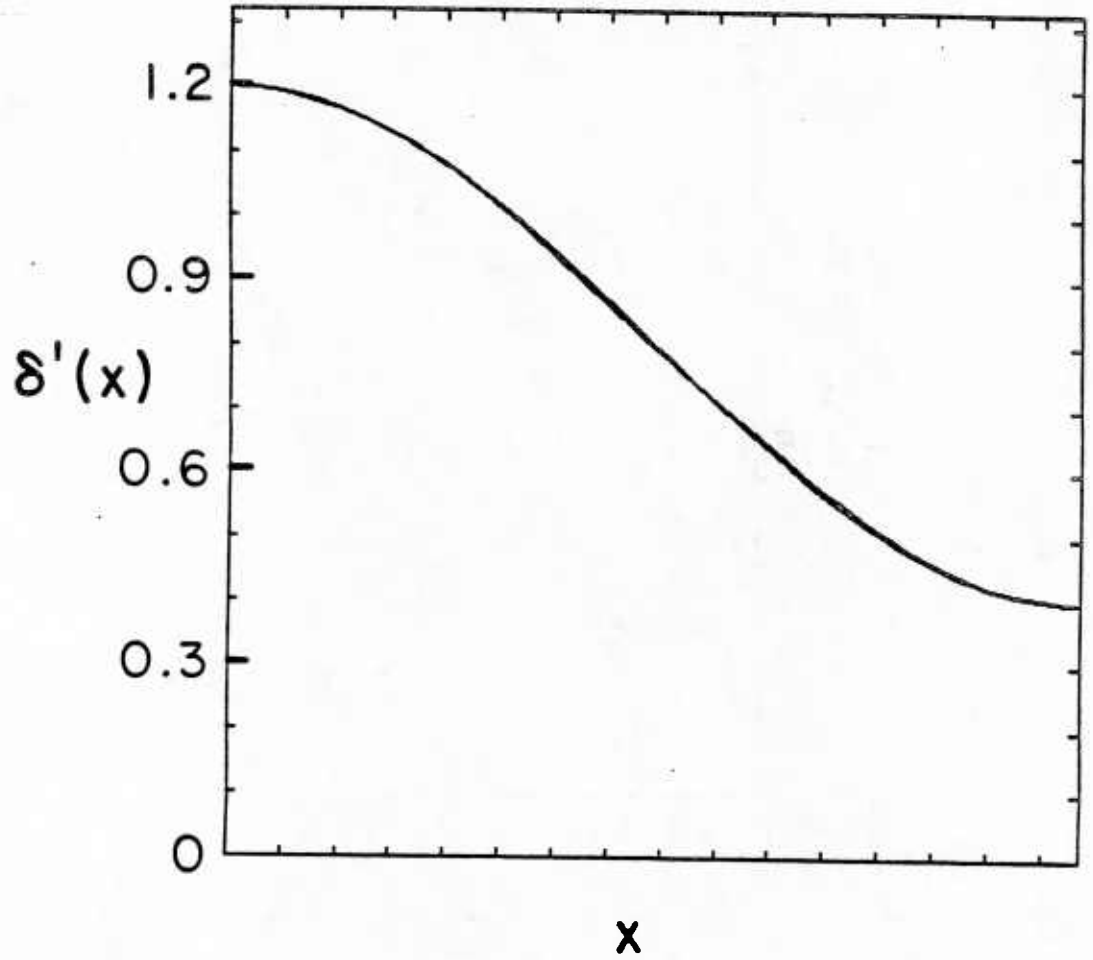
FIG. 12. Density as a function of the x coordinate at saturation of the field energy for (a) the background ions , (b) the stable beam ions and (c) the unstable beam ions. Only the unstable beam suffered nonlinear behavior. The parameters of Fig. 11 are used except $v_{ti}/U_b = 0.0$.
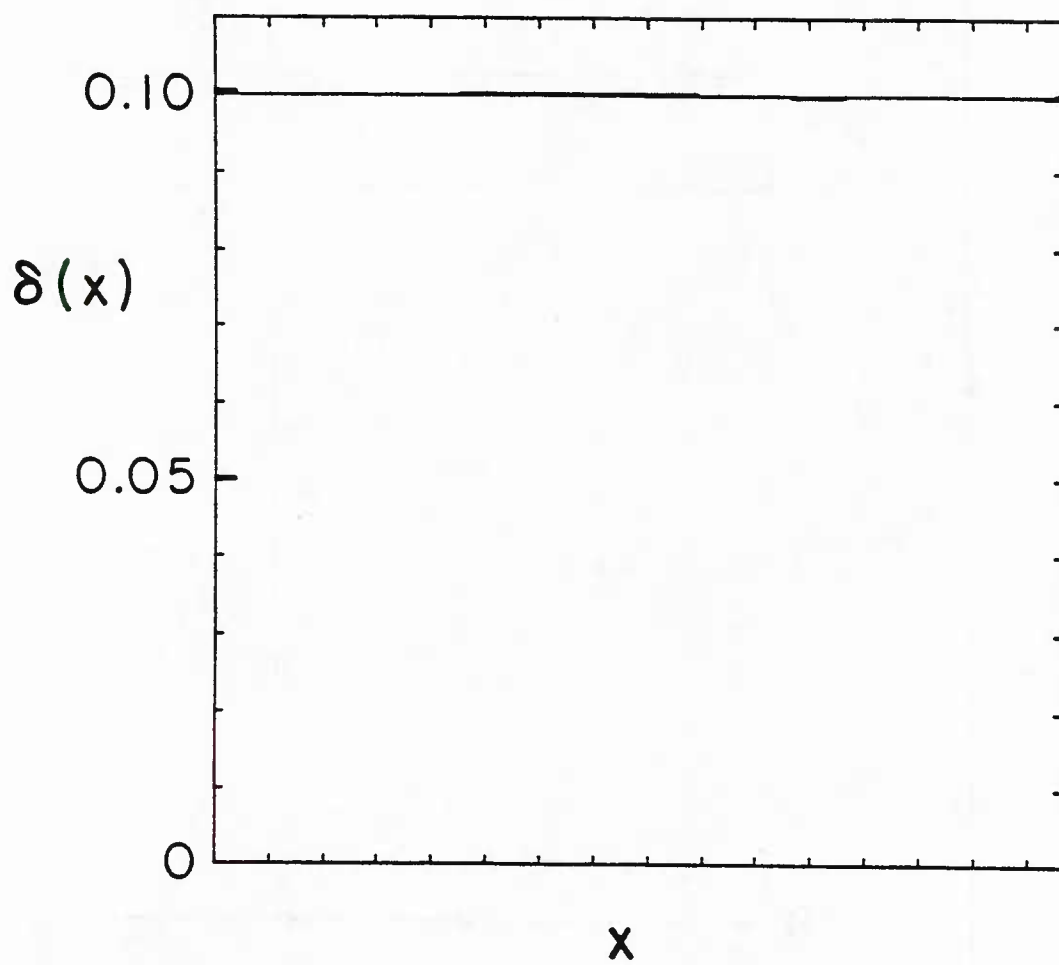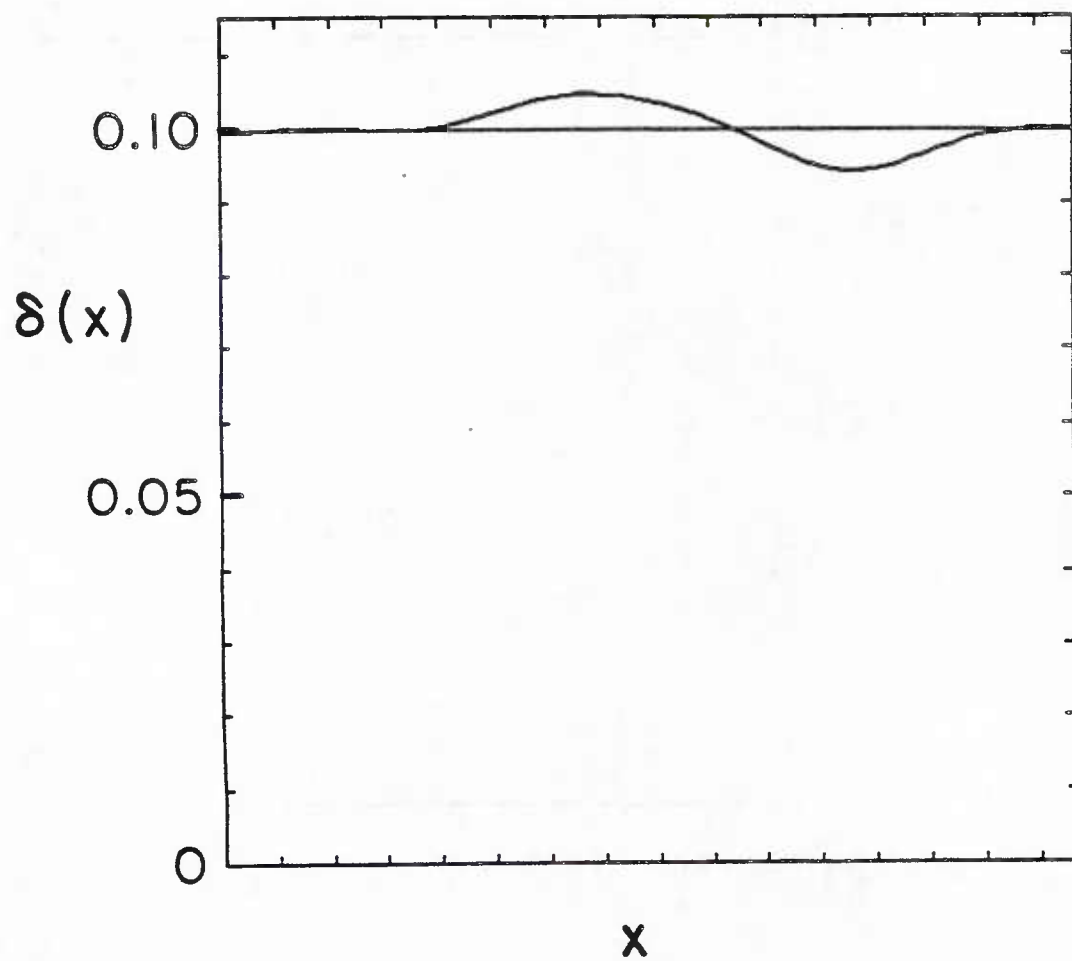
FIG. 12b.

FIG. 12c.
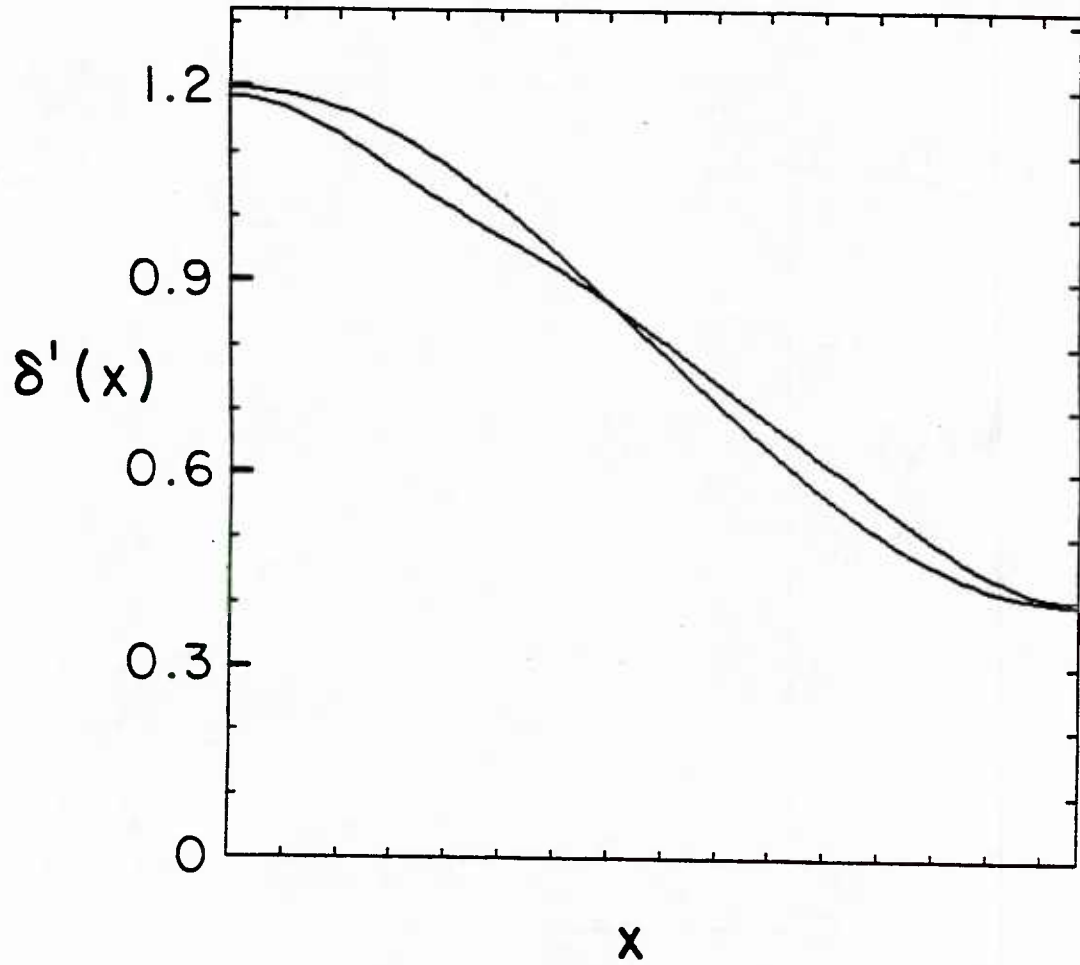
FIG. 13. Density as a function of the x coordinate at $t = 0$ (the cosine profile) and at saturation of the field energy for (a) the background ions , (b) the stable beam ions and (c) the unstable beams ions. Both the unstable beam and the background ions suffer non-linear behavior. The saturation value was $e\delta\phi/T_e = 0.28$.
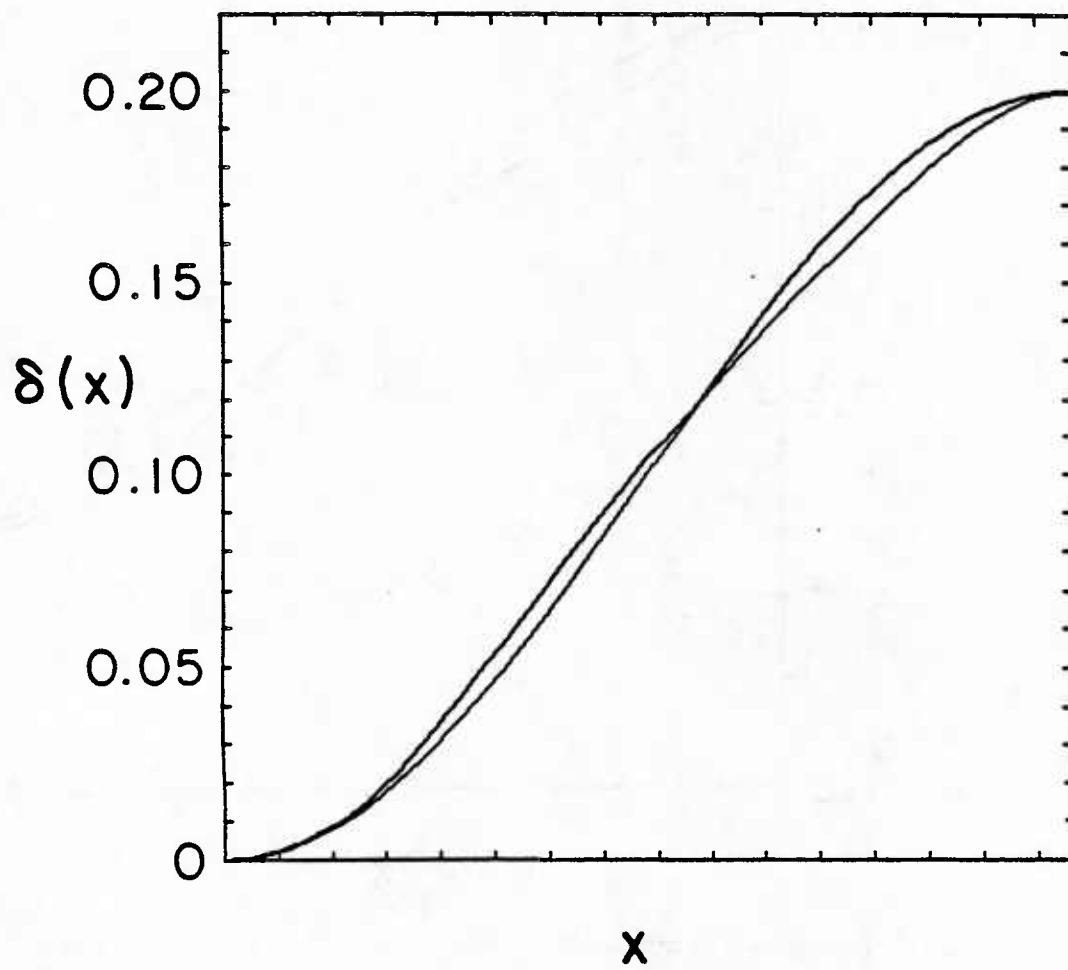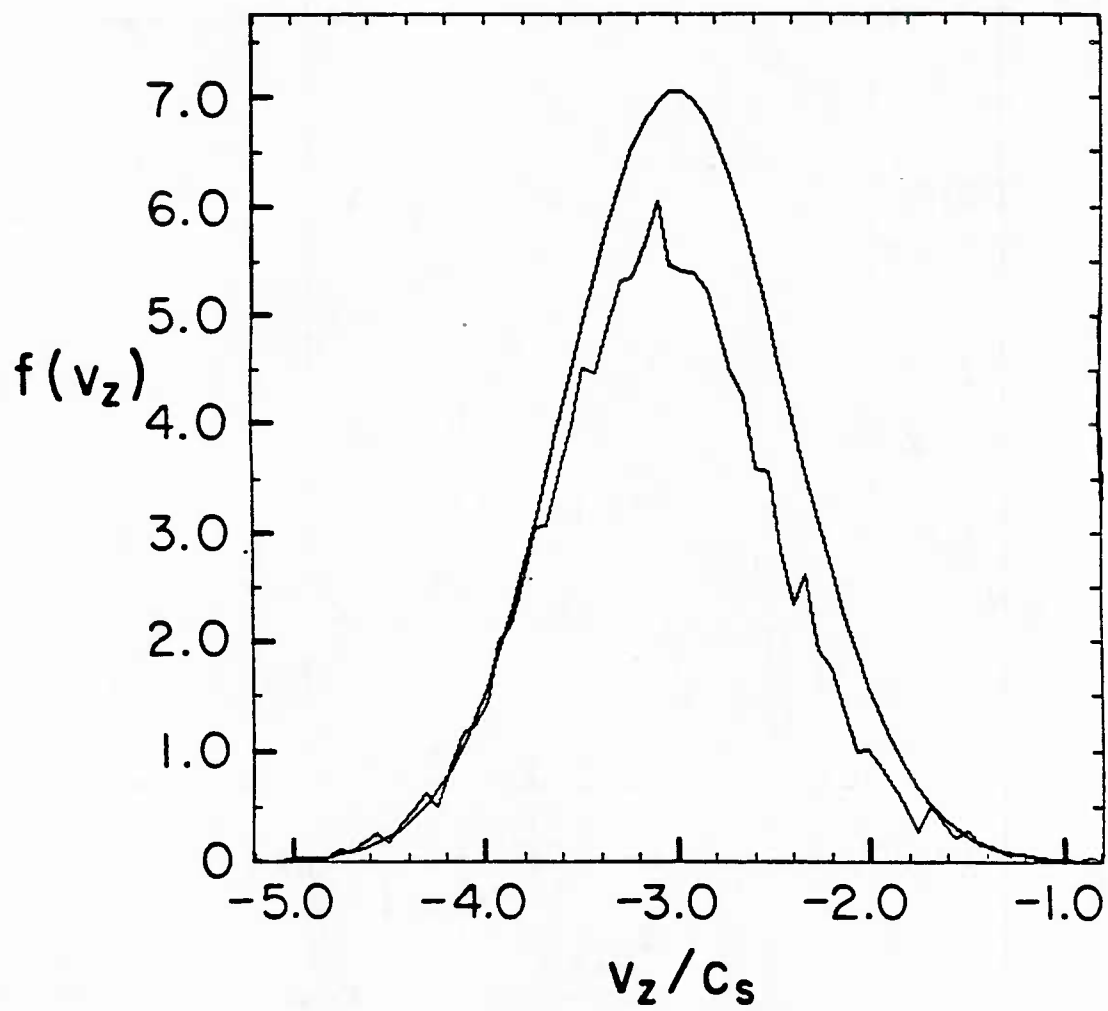
FIG. 13b.
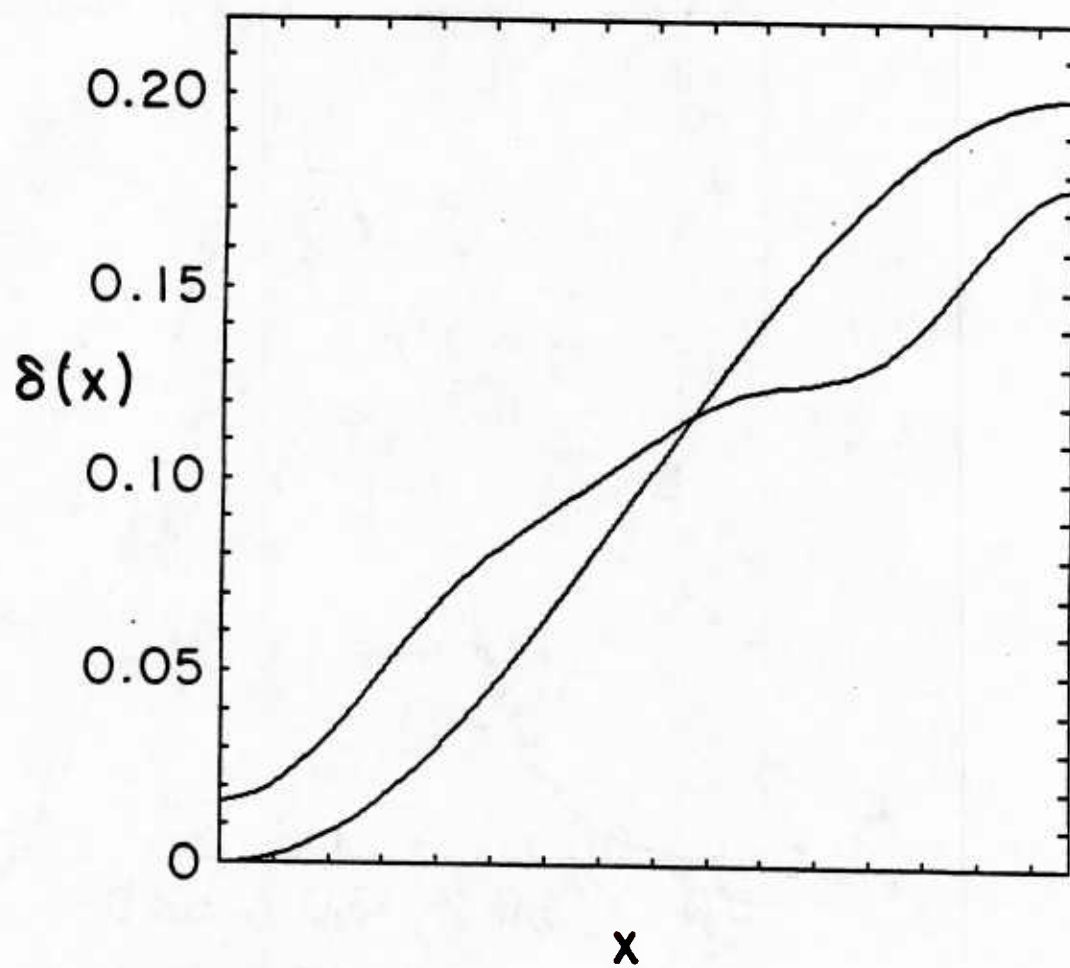
FIG. 13c.
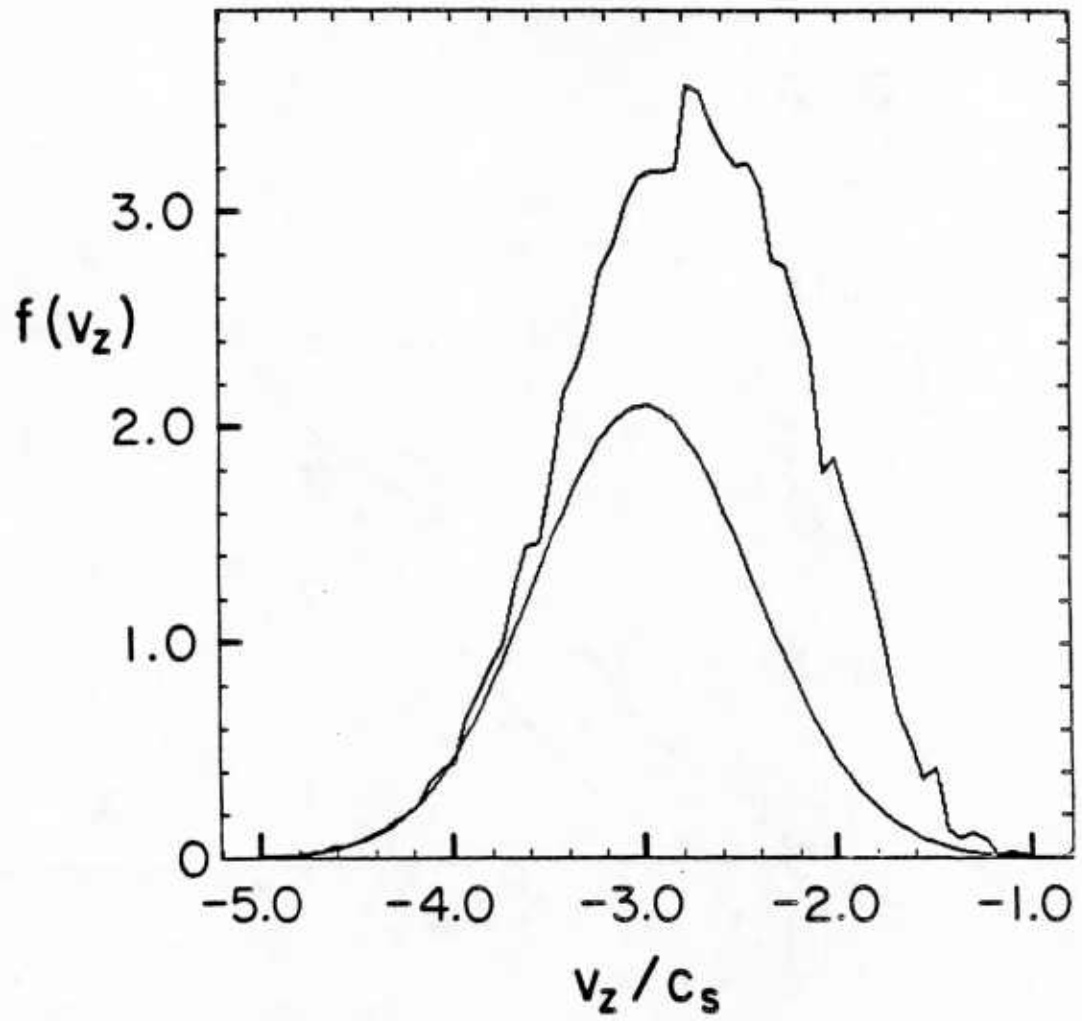
FIG. 14. Distribution function of the unstable ion beam averaged over 1/10 of the system length at $t = 0$ (the smooth curve) and at saturation (a) at the location $x_0/L_x = 0.3$ and (b) at the location $x_0/L_x = 0.7$.

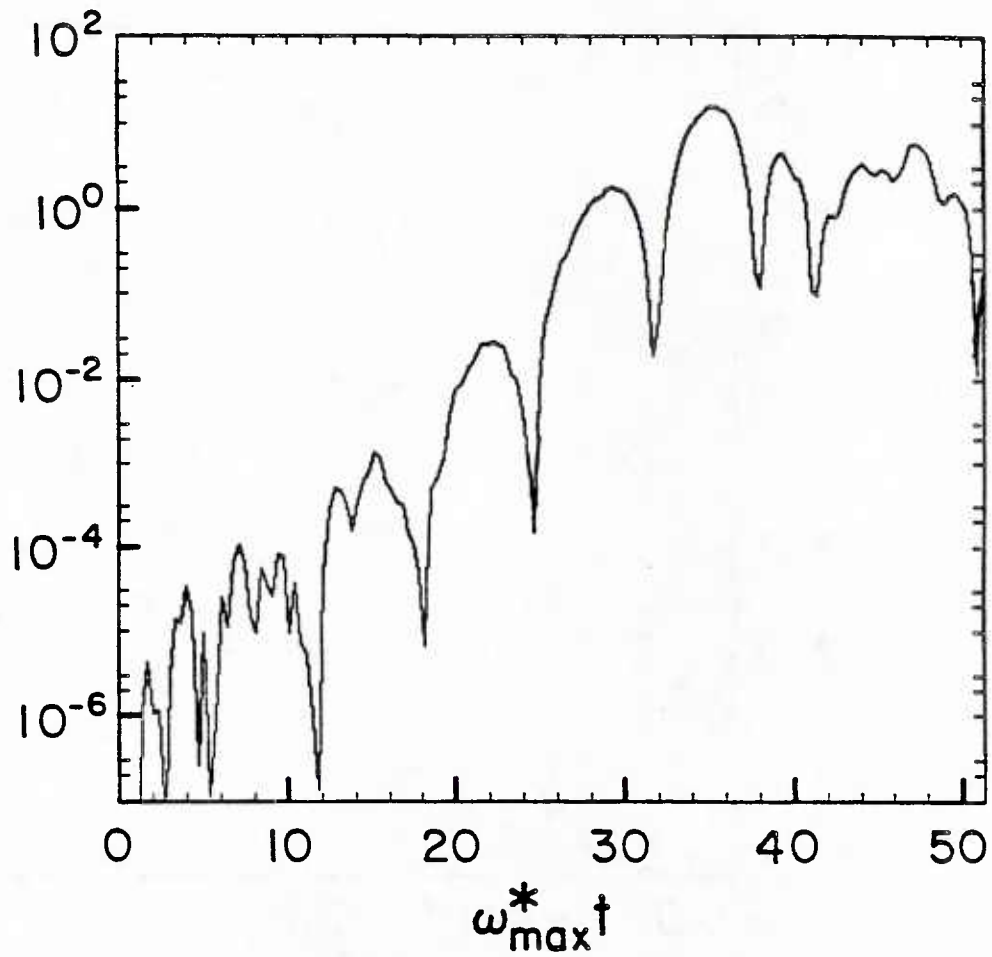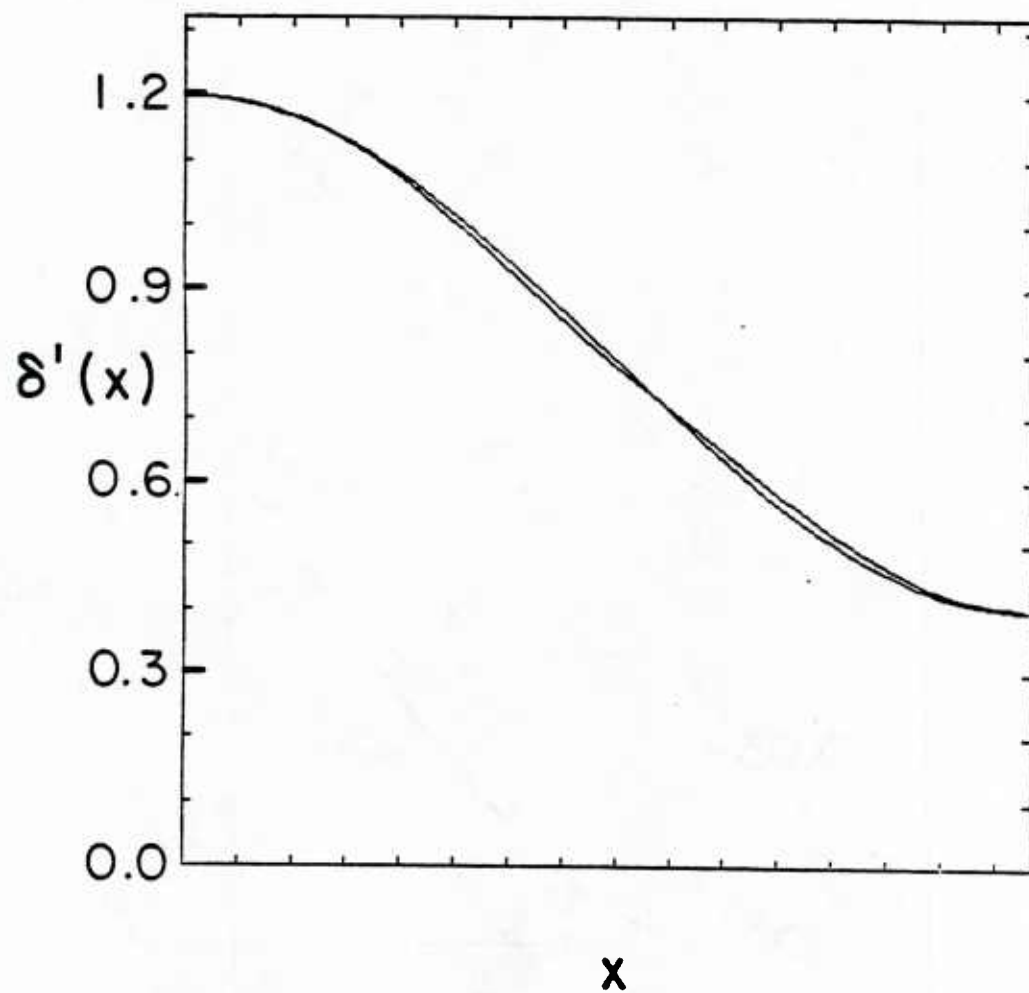FIG. 14b.

$$\text{Re}\left[\phi_{k_y, k_z}(x_0)\right]^2$$

FIG. 15. Time history of the square of the real part of the potential at a fixed location x_0. The parameters are the same as for Fig. 13 except that the 0th and 1th were kept in the periodic direction and the initial potential had the profile $\phi_0(x) = (T_e/e)(\,0.5 + 0.5\cos(\pi x/L_x))$.

FIG. 16. Density as a function of the x coordinate at $t = 0$ (the cosine profile) and at saturation of the field energy for (a) the background ion ions, (b) the stable ion beam and (c) the unstable ion beam. The parameters are the same as for Fig. 15. The saturation value is $e\delta\phi/T_e = 0.13$.
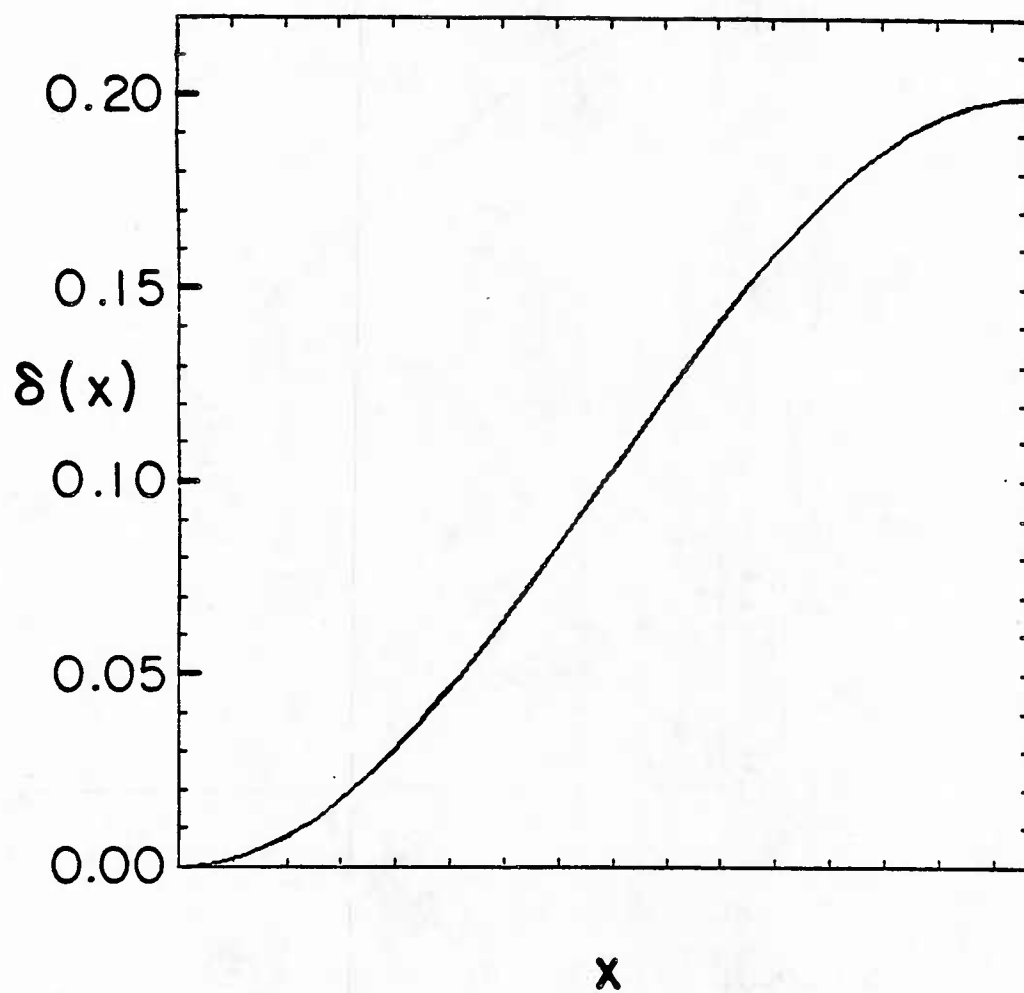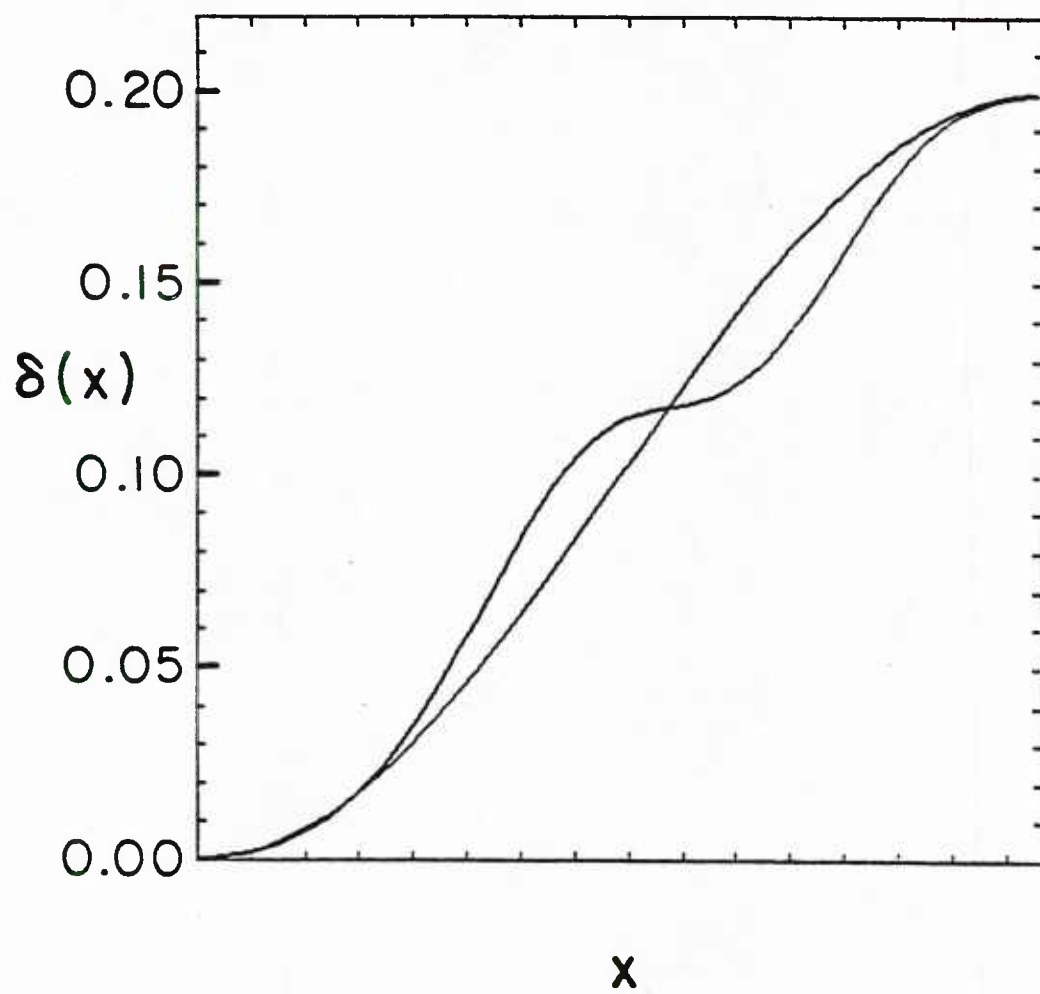
FIG. 16b.

FIG. 16c.